Allosteric and hyperekplexic mutant phenotypes investigated on an α1 glycine receptor transmembrane structure.

Gustavo Moraga-Cid, Ludovic Sauguet, Christèle Huon, Laurie Malherbe, Christine Girard-Blanc, Stéphane Petres, Samuel Murail, Antoine Taly, Marc Baaden, Marc Delarue, et al.

Allosteric and hyperekplexic mutant phenotypes investigated on an α_1 glycine receptor transmembrane structure.

Gustavo Moraga-Cid[1,2]*, Ludovic Sauguet[3,4]*, Christèle Huon[1,2]*, Laurie Malherbe[1,2,3,4], Christine Girard Blanc[5], Stéphane Petres[5], Samuel Murail[6], Antoine Taly[6], Marc Baaden[6], Marc Delarue[3,4#,] Pierre-Jean Corringer[1,2#]

1. Channel-receptors unit, Institut Pasteur, 75015 Paris, France.

2. Centre national de la recherche scientifique, CNRS UMR 3571, France

3. Structural dynamics of macromolecules, Institut Pasteur, 75015 Paris, France.

4. Centre national de la recherche scientifique, CNRS UMR 3528, France

5. Plateforme de Production de protéines recombinantes. Institut Pasteur. 75015 Paris. France

6. Therotetical biochemistry laboratory, IBPC, CNRS UPR9080, Université Paris Diderot Sorbonne Paris Cité, Paris, France

* Equal contribution

Correspondence should be addressed to delarue@pasteur.fr, pjcorrin@pasteur.fr

Abstract

The glycine receptor (GlyR) is a pentameric ligand-gated ion channel (pLGIC) mediating inhibitory transmission in the nervous system. Its transmembrane domain (TMD) is the target of allosteric modulators such as general anesthetics and ethanol, and is a major locus for hyperekplexic congenital mutations altering the allosteric transitions of activation or desensitization. We previously showed that the TMD of the human α_1GlyR could be fused to the extracellular domain of GLIC, a bacterial pLGIC, to form a functional chimera called Lily. Here, we overexpress Lily in S2 insect cells and solve its structure by X-ray crystallography at 3.5 Å resolution. The TMD of the α_1GlyR adopts a closed-channel conformation involving a single ring of hydrophobic residues at the center of the pore. Electrophysiological recordings show that the phenotypes of key allosteric mutations of the α_1GlyR, scattered all along the pore, are qualitatively preserved in this chimera, including those that confer decreased sensitivity to agonists, constitutive activity, decreased activation kinetics or increased desensitization kinetics. Combined structural and functional data indicate a pore opening mechanism for the α_1GlyR suggesting a structural explanation for the effect of some key hyperekplexic allosteric mutations. The first X-ray structure of the TMD of the α_1GlyR solved here using GLIC as a scaffold paves the way for mechanistic investigation and design of allosteric modulators of a human receptor.

Significance

Pentameric ligand-gated ion channels (pLGICs) mediate neuronal communication in the central nervous system. Upon the neurotransmitter binding, these receptors undergo a rapid conformational change to open an integral ion channel. Mutations impairing the function of pLGICs are known to cause hyperekplexic, myasthenic and epileptic syndromes. Here, we studied how the local perturbations caused by single mutations result in an alteration of the protein function. Using a chimeric protein assembled by the transmembrane domain of the human glycine receptors fused to the extracellular domain of the bacterial pLGIC GLIC we performed functional experiments in parallel with X-ray crystallography. On this basis, we propose a molecular mechanism for channel opening that accounts for the phenotypes of several mutants causing hyperekplexia.

Introduction

The Glycine receptor (GlyR) belongs to the superfamily of pentameric ligand-gated ion channels (pLGICs) which plays a key role in neuronal communication (1). In humans, this superfamily includes nicotinic acetylcholine (nACh), serotonin ($5HT_3$) and γ-aminobutryic acid ($GABA_A$) receptors. pLGICs are pentamers where each subunit is composed of an extracellular domain (ECD), a transmembrane domain (TMD) made of four helices M1-M4, and an intracellular domain (ICD). Neurotransmitter binding within the ECD triggers receptor activation, resulting in channel opening in the TMD, followed by desensitization (1). These allosteric transitions are at the heart of pLGIC function under normal conditions.

In addition, point mutations altering the conductance of the channel, or more frequently the isomerization constants and/or kinetics between the allosteric states, cause congenital hyperekplexic, myasthenic and epileptic syndromes (2). Hyperekplexia is a rare inherited neurological disorder characterized by noise- or touch-induced non-epileptic seizures and excessive muscle stiffness. It is mainly caused by mutations in the α_1GlyR subunit, which forms functional homomeric receptors as well as heteromeric receptors in association with the βGlyR subunit (3). While numerous hyperekplexic mutations have been extensively studied in recombinant systems, the molecular basis of their effects has remained elusive.

The last decade has seen decisive progress in the determination of X-ray structures of pLGICs (1). The acetylcholine binding proteins (AChBPs) homologous to the pLGIC-ECDs were first solved (4), followed by two bacterial homologs called ELIC (5) and GLIC (6). GLIC is activated by protons, and its crystallization under conditions favoring the resting (GLIC-pH7) (7) or the active (GLIC-pH4) (6, 8, 9) states revealed its gating mechanism. The ECDs of subunits that are loosely packed at pH7 come closer according to a “blooming” motion following acidification, in concert with channel opening that involves a major tilt of the M2 channel-lining helix. Crystallization of several GLIC mutants revealed a locally-closed “GLIC-LC” state resembling the open form but where the M2 helices are arranged like in the GLIC-pH7 form (7, 10, 11). Recently, three structures of eukaryotic pLGICs have been

solved: the GluCl receptor from C. elegans (12, 13), the human β_3GABA$_A$R (14), and the rat 5HT$_3$R (15), revealing a high conservation of the core structure of pLGICs from bacteria to animals. Interestingly, the GluCl receptor was solved in a closed (13) and open (12) conformation. Comparison of the two forms shows a reorganization of the ECD resembling that of GLIC, but at the TMD channel opening results from a global tilt of each subunit four helix bundle, that contrasts with the local tilt of M2 found in GLIC.

To develop a versatile method for collecting high-resolution structural data of human pLGICs, we used GLIC as scaffolding protein to host TMDs from other receptors and solve their structure. Indeed, GLIC crystal packings involve mainly interactions between the ECD and the short cytoplasmic M3-M4 loop, but only limited interaction with the TMD, largely shielded from the solvent by the detergent. In previous work, we designed a chimera composed of the ECD of GLIC fused to the TMD of the human α_1GlyR, where the ICD of the α_1GlyR was replaced by the short linker (SQP motif) found in GLIC (16). In this chimera, mutations Y119F and F121M were introduced (loop 7) and the C-terminal tail of the α_1GlyR was substituted to that of GLIC to increase the structural complementarities between the ECD and the TMD. This construct, here called Lily (GLIC-GlyR, Figure 1A-D) functions as a proton-gated ion channel and displays a transmembrane pharmacology and ion channel properties closely resembling those of the α_1GlyR.

Here, we solved the structure of Lily allowing us to reinvestigate the phenotype of several α_1GlyR allosteric mutants, and to propose a gating mechanism based on the new X-ray structure.

Results

1- Over-Expression of Lily-His in a Functional State

In contrast to GLIC, we found that Lily does not overexpress in *E. coli*. We thus expressed Lily in *Drosophilia* Schneider 2 (S2) cells with a Gly-Gly-$(His)_{10}$ tag at its C-terminus (Figure 1, S1A). We checked that S2 cells expressing both Lily-His and GLIC-His yielded robust proton-elicited currents (Figure 1D), characterized by EC_{50}s for proton activation of 4.1 ± 0.3 x 10^{-6} M (pH 5.3) and 4.8 ± 0.6 x 10^{-6} M (pH 5.3), respectively. At pH 5, application of the channel blocker picrotoxinin (100 µM) yielded a 91 ± 7% inhibition of the Lily-His currents showing the specificity of the response. For the mutational studies showed below, we recorded Lily and GLIC in BHK cells with a C-terminal HA tag (16) which does not alter the electrophysiological response (17), yielding EC_{50}s of 3.3 ± 0.1 × 10^{-7} M (pH 6.5) and 4.8 ± 0.6 x 10^{-6} M (pH 5.3), respectively.

2- X-ray Structure of Lily-His in the Locally-Closed Conformation

Lily-His was purified in dodecylmaltoside and subjected to extensive crystallization trials. The best crystals were obtained at pH 3 (similar crystals were obtained at pH 4, albeit diffracting to lower resolution). Lily-His was solved at 3.5 Å with I/σ of 1.2 in the highest resolution shell (Table S1) in a $P2_12_12_1$ type crystal packing (Figure S1 B,C). NCS symmetry averaging improved the quality of the electron density allowing the unambiguous reconstruction of the peptide backbone except for the first four N-terminal residues, the short M1-M2 loop (residues 218-222) and the C-terminal histidine tag (Figure 2A,B,D). The quality of the electron density at the bottom of the TMD and at the top of the M3 and M4 helices is lower. At these levels several side chains, representing a third of the TMD residues, could not be built unambiguously and were omitted in the model. (Figure S2 A,B).

Lily-His adopts the same locally-closed conformation as GLIC-His, with a Cα rmsd between the two structures of 0.68 Å (0.43 Å in the ECD and 0.85 Å in the TMD, Figure 2C) indicating a quasi-identical backbone conformation of the two proteins, notably of the four transmembrane helices and of the M2-M3 loop. Concerning GLIC-His, solved in the same crystal packing at a similar resolution (3.35 Å) (7), most of the side chains could be modeled from the electron density map. This indicates that, in

this crystal, the TMD of the α_1GlyR is more flexible than the TMD of GLIC, a feature supported by the high B factor of the TMD of Lily as compared to its ECD (200 ± 4 $Å^2$ vs 160 ± 12 $Å^2$). The lower thermostability of Lily-His in detergent solution (42°C) compared to GLIC-His (52°C) (Figure S2 C) is consistent with these observations.

2.1- Ion channel structure: The ion channel is closed in the Lily structure (Figure 3A): the ring of L261(9') residues forms a tight hydrophobic constriction of 2.2 Å diameter constituting the gate of the channel (the main barrier to ion translocation). Above, rings of T264(13') and S268(16') form a wider hydrophilic pore (6.1 and 7.1 Å diameter, respectively). A similar architecture is observed in the closed structure of the GluCl-Apo receptor, in contrast to bacterial cationic pLGICs that display a larger diameter at L261(9') but carry an extended hydrophobic gate at positions 13' or 16' (see Figure S3A for GluCl-Apo, GLIC-pH7 and ELIC structures). As no second hydrophobic barrier exists, the highly constricted barrier at the L261(9') level might be necessary to seal the channel and prevent any ion conduction. These data suggest a similar gate in the GlyR and GluCl receptors that are closely related in terms of sequence and ion channel properties. Finally, the upper turn of the M2 helix is partially broken in Lily, carrying the R271(19') residue that forms a polar/positively charged constriction of 2.8 Å diameter. Below the L261(9') position, the B-factor progressively increases when going down through T258(6'), G254(2') and P250(-2'), to reach the short disordered M1-M2 loop.

2.2- Inter-helices interactions: The structure reveals a set of side-chain interactions that are specific to the α_1GlyR (Figure 3B). At the tip of M2, the carboxylate of E243(GLIC) and the guanidinium moiety of R271(Lily) point toward the adjacent M2 helix and elicit quaternary hydrogen bonding with the main chain carbonyl of the 17' residue. The K248(GLIC)/K276(Lily) (24') side chain points toward E243(19') and is well resolved in GLIC, while it is resolved in only one out of five chains in Lily and points in the opposite direction. This suggests electrostatic attraction/repulsion between K248(GLIC)/K276(Lily)(24') and E243(GLIC)/R271(Lily)(19'). The tip of M1 interacts with the C-terminus of the M2-M3 loop in Lily through hydrophobic interactions between I225 and V280 while no such interaction occurs in GLIC.

2.3- ECD/TMD coupling interface: The coupling region essentially consists in intra-subunit interactions between the lower part of the ECD (Loop 2, Loop 7 and pre-M1)

and the upper part of the TMD (M2-M3 loop). 10 out of 15 interfacial residues are conserved between GLIC-LC and Lily (Figure S3B), resulting in the conservation of key interactions, notably hydrophobic stacking of P247(GLIC)/P275(Lily) with F116 and Y(GLIC)/F(Lily)119 (Figure 3B). In both structures, the side chain of L246(GLIC)/L274(Lily) points toward hydrophobic residues from the TMD. In the M2-M3 loop, the phenol moiety of Y251(GLIC)/Y279(Lily) is stacked with the guanidinium moiety of R117. This overlapping set of interactions at the ECD/TMD interface provides a structural explanation for the compatibility of the GLIC-ECD and the α_1GlyR-TMD to form a functional channel.

Non-conserved GLIC/Lily residues are T253/K281, Y254/A282, Y119/F119, F121/M121 and Y194/M220 (Figure S3B). They do not impair the allosteric coupling, but certainly modulate the functional properties. For instance, we showed that performing the F119Y and M121F mutations on Lily results in an acceleration of the desensitization kinetics (16). Extensive mutagenesis work has shown that the entire interface is involved in fine tuning of the allosteric response to agonist (18,19).

3- Electrophysiological Analysis of Allosteric Mutants in Lily

We reinvestigated the effect of well-characterized α_1GlyR mutations by patch-clamp electrophysiology on Lily-HA and α_1GlyR in BHK cells. We selected 7 mutants, localized in various regions of the TMD: upper part of M1 behind the gate (Q226E), lower part of the channel (P250T and G254A), upper part of the channel (Q266E and R271Q) and M2-M3 loop (K276C and V280M) (Figure 4A). Except for Q266E and G254A, all mutations are associated with autosomal dominant hyperekplexia.

On Lily, R271Q produces a 10-fold increase in EC_{50} for protons with a 1.5-fold decrease in maximal currents and a reduction in unitary conductance (from 86 ± 2 pS in WT to 56 ± 3 pS) (Figure 4B, S4E). On the α_1GlyR, we observe a more marked 450-fold increase in EC_{50} for glycine (Figure S4 A,B,C), in agreement with previous works, that also report a reduced single channel conductance (20, 21). The phenotype of R271Q is thus similar in Lily and α_1GlyR, although a stronger effect on the agonist EC_{50} is found for α_1GlyR. Interestingly, the R271 residue in Lily appears close enough to elicit long-range electrostatic interaction with the K33 residue from the ECD, while a Thr is found at this position in the α_1GlyR. The different side-chain

environment may contribute to the difference in phenotypes between both receptor types.

Recently, Q226E was reported to produce spontaneously open channels (22, 23). On Lily, this mutation equally produces constitutive opening: 1) Immediately after the whole-cell clamping at pH 8.0, cells expressing Q226E generate high leak currents,(~600 pA) that are blocked by 100µM of picrotoxin. Application of a more acidic solution further increases the currents, but the bad shape of the cells precluded repetitive stimulations and measurement of dose-response curves. 2) Single-channel recording at pH 8.0 shows repetitive spontaneous openings (Figure 4C), whereas no spontaneous activity is observed for Lily-WT.

On the α_1GlyR, mutant cycle analysis suggests that Q226E stabilizes the active state through enhanced electrostatic attraction to R271 (22). We investigated this possibility on Lily. We observe that Q226E/R271Q no longer displays spontaneous currents, but a 570-fold increase in the EC_{50} for protons as compared to WT (Figure 4B, S4F). It is not possible to measure the EC_{50} of Q226E, but assuming a value around pH 8 as judged from single channel traces, mutant cycle analysis yields strong energetic coupling between Q226E and R271Q (15 KJ mol^{-1}). This suggests that both positions interact through electrostatic forces to stabilize the open conformation. On the α_1GlyR, R271Q and Q226E/R271Q both produce an increase in EC_{50}, but the extents of their effects are significantly different from that found in Lily, pointing this time to a near-additive effect of R271Q and Q226E (Figure S4G and S5). We also introduced a glutamate at a different position nearby R271. On Lily, Q266E produces a 3.3-fold increase in sensitivity to protons (Figure 4D). Combining Q266E with R271Q results in a 230-fold decrease in proton sensitivity, again indicating energetic coupling between the two positions (10 KJ mol-1). However, performing the same set of mutations on the α_1GlyR also points to an additive effect due to the different R271Q phenotype (Figure S5 D-F). The quantitative differences between the phenotypes of the R271Q and Q226E/R271Q in Lily and the α_1GlyR may tentatively be accounted by the fact that, for Lily, proton activation may involve the titration of transmembrane residues interacting with the E226/R271 cluster. Indeed, recording of the α_1GlyR R271Q and Q226E/R271Q mutants at pH 5 indicates a significant alteration of the dose-response curves (Figure S5 A-C). In

conclusion, the analysis on Lily shows coupling energy between Q226E/R271Q and to a lesser extent Q266E/R271Q, but these features are not unraveled on the α1GlyR possibly due to a different mode of activation.

In the M2-M3 loop, we found that K276C on Lily produces a 120-fold increase in EC_{50} and a large reduction of the maximal currents (Figure 4E, S4D,E). This phenotype is similar to what is found in the α_1GlyR (24, 25). Likewise, V280M (28) was reported to produce a strong gain of function; we observed a phenotype similar to Q226E bearing spontaneous activity at pH8 (Figure 4F).

At the bottom of the channel, P250T confers reduced glycine sensitivity and increases the rate of desensitization on the α_1GlyR (Table S2) (26). On Lily, P250T produces a very similar phenotype characterized by: 1) a marked increase in desensitization kinetics, with current traces displaying a 20% vs. an 80% decay upon 1s application of proton at pH 4 for WT and P250T, respectively (Figure 5A,C); 2) a 46-fold increase in EC_{50} for protons (Figure 5B), and 3) a 5-fold reduction of the maximal currents. Second, the α_2GlyR displays slow kinetics of activation and a large conductance in the 100–120 pS range (27). The M2 helix of α_1 and α_2 GlyRs are identical except at position 254 (Lily numbering) (α_1Gly and α_2Ala). We thus performed the G254A mutation on Lily (Figure 5D-F), showing a marked reduction of the rate of activation evaluated by following the onset of the whole-cell current traces (at pH 5.0 τ_{act}= 950 ± 62 ms vs. 64 ± 6.6 ms for G254A and WT, respectively). Moreover, the G254A mutant shows an increase in single channel conductance (125 vs. 86 pS).

Overall, except for mutants R271Q and Q226E/R271Q, this data points to a similar phenotype when equivalent mutations are performed on Lily and on α_1GlyR.

Discussion

1- A modular architecture for pLGICs

The early observation that the α_7nAChR(ECD)-5HT_3R(TMD+ICD) chimera was functional was the first evidence that the ECD and TMD may constitute independent tertiary modules (28). The α_7nAChR(ECD)-α_1GlyR(TMD+ICD) (18), the AChBP-5HT_3(TMD+ICD) (29), and recently the ELIC(ECD)-α_7nAChR(TMD) chimera (30) were subsequently reported to be functional, the ECD retaining "native-like" pharmacology for agonists and the TMD "native-like" channel selectivity. It is noteworthy that extensive mutations at the ECD-TMD interface were required to produce properly folded and/or functional AChBP-5HT_3(TMD+ICD) and ELIC(ECD)-α_7nAChR(TMD) chimeras.

A conserved modular architecture of pLGICs from bacteria to humans is now established by all available X-ray structures. Interestingly, the two domains of Lily, when expressed alone, were previously found to self-assemble. First, we showed that the isolated ECD of GLIC folds as a soluble monomer and its X-ray structure confirmed it retains the usual β-sandwich fold (331). Second, an ensemble of 15 models of the α_1GlyR TMD expressed alone and refolded in lipidic micelles has been solved by a combination of electron microscopy (EM) and nuclear magnetic resonance (NMR) (32). The former shows in majority a pentameric assembly and the latter a bundle of 4 helices for each chain. However, these models show marked difference with the Lily TMD structure, a feature possibly due to lack of structural constraints applied by the ECD (for discussion, see Figure S6 A-B and legends).

These data suggest a maturation pathway of Lily that would explain the striking compatibility between ECDs and TMDs from different pLGICs, even when separated by billions of years of evolution. The ECD and TMD of Lily would fold autonomously, followed by the assembly of the TMD into a pentamer, triggering subsequent pentamerization of the ECD. This scheme may be extended to other pLGIC subtypes since other domains were found to self-assemble, including the ECD of the α_1nAChR (33), and the isolated TMDs of the $\alpha_4\beta_2$ and α_7 (34) nAChRs.

2- A plausible gating mechanism of the TMD of the α_1GlyR

Our electrophysiological analysis showed that the TMD of Lily displays an ion channel indistinguishable from that of the α_1GlyR in terms of conductance and selectivity, and a pharmacology for general anesthetics, alcohols, and ivermectin similar to that of the α_1GlyR (16). We show here that the phenotypes for key allosteric mutations, scattered at different locations within the TMD are similar on the α_1GlyR and Lily. In addition, those phenotypes involve all aspects of the activation transition, including 1) increase or decrease of the isomerization constant between resting and active state (causing decreased agonist sensitivity (R271Q and K276C) and constitutive opening (Q226E and V280M), respectively), 2) alteration of activation kinetics (in G254A) and 3) single channel conductance (R271Q and G254A). This indicates that those residues experience similar changes in microenvironment during activation in both Lily and the α_1GlyR. Concerning desensitization, our data also suggest a preserved mechanism thanks to the conservation of the phenotype of P250T. These data suggest a similar gating reorganization of the TMD in Lily and in the α_1GlyR.

Here, Lily is expressed as a functional channel and crystallized in the LC conformation. For GLIC, the LC form corresponds globally to the open form, but a concerted bending of the upper part of the all M2 helices obstructs the pore by forming a tightly packed bundle, along with a revolving motion of the M2–M3 loop that is similar to what is observed in the pH7 conformation. Therefore, the conformation of the TMD in the LC form is similar to the pH7 resting form, with the exception of the M1 helix showing a 10° hinge motion in its upper half. We built a “completed X-ray structure” model of the TMD of Lily by adding the missing side chains and the backbone atoms of the five missing residues to the X-ray structure. We verified that a homology model of Lily based on GLIC-pH7 shows a TMD conformation (Figure S6B) similar to that of the completed X-ray structure (figure 6 A,B,C).

Concerning the open state, the available structural data of pLGICs show a similar TMD structure of GLIC and of the GluCl receptor. GLIC and the GluCl receptor are phylogenetically close to the α_1GlyR (sharing respectively 34% and 26% amino acid identity at the TMD), supporting the idea that they are good models for the open form of the α_1GlyR at the TMD. We therefore built a homology model of the open

conformation of Lily based on GLIC-pH4. We chose GLIC-pH4 because its open channel structure was not constrained by ivermectin.

Assuming a common gating pathway between GLIC and the α_1GlyR, we can use the completed X-ray structure and the homology open model as templates to investigate the activation transition of the α_1GlyR TMD (Figure 6). According to this "Lily" gating model, channel opening is caused by a tilt of the upper-half of each M2 helix. In the process, M2 comes closer to M3 from the same subunit and to M1 from the adjacent subunit. This mechanism is consistent with a wealth of biochemical and mutational data collected on various pLGICs (7). In particular, it accounts for the phenotype of cross-linked double cysteine mutants, which show that M2 comes closer to M3 during activation in both GLIC and the α_1GlyR (10, 35).

3- Structural interpretation of allosteric mutant phenotypes

For Lily, electrophysiological data points to an electrostatic interaction between R271 and E226 to stabilize the open state. In the open model of Lily, both residues are close enough to interact through a salt bridge, while they are far away in the closed form, suggesting that E226 stabilizes the open channel though "pulling" R271, at the tip of M2, away from the 5-fold symmetry axis to interact with M1. On the α_1GlyR, the Q226E and R271Q mutations do not reveal coupling energy between the 2 positions, but a series of other mutations support the above conclusion (22). Data were previously interpreted on the basis of a speculative gating model between ELIC (closed) and GLIC (open) (22, 23), where M2 and M3 tilt altogether as a rigid block. Here we provide a different gating model supported by a combination of electrophysiological, X-ray and modeling data that mainly involves motion of M2 alone (Figure 6C,F; S7).

In addition, the V280 residue is an interesting reporter as it is located in the M2-M3 loop that undergoes a key revolving motion during gating. V280 interacts with I225 from the upper part M1, a helix portion directly linked to the ECD and involved in signal transduction. In the α_1GlyR, the spontaneous currents of V280M were correlated with an increased volume of the side chain (22). In the gating model, the upper part of M1 moves away from M3 in the course of channel opening, resulting in an increased distance between V280 and I225 (a Cβ-Cβ distance increase from 5.7

to 6.6 Å). Bulkier residues at position 280 are thus expected to stabilize the open form, providing a structural explanation for the observed phenotypes (Figure 6B,E).

We further show a loss-of-function phenotype for the K276C mutation on Lily, whereas the homologous K248C mutation on GLIC has an opposite effect yielding a 20-fold increase in proton sensitivity (10). This conserved Lys side chain points in different orientations in both structures (Figure 3B). In GLIC, it projects toward the upper part of M2, possibly making a salt bridge with E243, whereas in Lily, it projects between helices M1 and M2 from the adjacent subunit, possibly because of electrostatic repulsion with R271. The markedly different orientations of this otherwise conserved residue provide a rationale for the opposite phenotypes observed by electrophysiology.

Conclusion

The receptor engineering approach based on functional chimeras presented here allowed us to solve the structure of the TMD of the α_1GlyR, and should be easily extended to other pLGICs. The Lily structure may help the drug design of allosteric effectors acting at the α_1GlyR TMD. For instance, comparison of the open and closed models of Lily shows a reorganization of the intersubunit pocket that is lined by the S268 and A288 residues and mediates allosteric potentiation of the α_1GlyR by general anesthetics and ethanol (36). The pocket markedly narrows down in the open-channel form, providing a plausible mechanism whereby it contracts around the effector to facilitate activation (Figure 6D,G). We also demonstrate that Lily is a pertinent model for studying the molecular mechanisms underlying allosteric mutations that may be ultimately beneficial for patients suffering hyperekplexia.

Materials and Methods

Lily was expressed and purified as in ref. (7). Crystals were obtained using vapor diffusion. The (6–8 mg/ml) protein was mixed in a 1:1 ratio with reservoir solution containing 16–20% PEG 2000MME, 50 mM NiCl2, 4% DMSO, 11% ethylene glycol and 0.1 M NaAcetate pH 3.0. Coordinates and structure factors were deposited with PDBid 4X5T. Whole cell and single channel patch-clamp electrophysiology was

performed as previously described (16). Details are provided in supplementary information.

Acknowledgments: we acknowledge financial support by the fondation de la recherche médicale (GMC), the DARRI (Institut Pasteur), and the Agence Nationale de la Recherche (“Nicochimera”). The "Initiative d'Excellence" (Grant "DYNAMO", ANR-11-LABX-0011 to SM, AT and MB). Fondation Pierre-Gilles de Gennes pour la Recherche (SM).

References

1. Corringer PJ, Poitevin F, Prevost MS, Sauguet L, Delarue M, *et al* (2012) Structure and pharmacology of pentameric receptor channels: from bacteria to brain. Structure 20(6):941-956.
2. Galzi JL, Edelstein SJ, Changeux JP (1996) The multiple phenotypes of allosteric receptor mutants. *Proc Nat Acad Sci U S A* 93(5):1853-1858.
3. Davies JS, Chung SK, Thomas RH, Robinson A, Hammond CL, *et al* (2010) The glycinergic system in human startle disease: a genetic screening approach. Front Mol Neurosci 23(3):8.
4. Rucktooa P, Smit AB, Sixma, TK (2009) Insight in nAChR subtype selectivity from AChBP crystal structures. Biochem Pharmacol 78(7):777-787.
5. Hilf RJ, Dutzler R (2008) X-ray structure of a prokaryotic pentameric ligand-gated ion channel. Nature 452(7185):375–379.
6. Bocquet N, Nury H, Baaden M, Le Poupon C, Changeux JP, *et al* (2009) X-ray structure of a pentameric ligand-gated ion channel in an apparently open conformation. Nature 457 (7225):111–114.
7. Sauguet L, Shahsavar A, Poitevin F, Huon C, Menny A, *et al* (2014) Crystal structures of a pentameric ligand-gated ion channel provide a mechanism for activation. Proc Natl Acad Sci U S A 111(3):966-971.
8. Sauguet L, Poitevin F, Murail S, Van Renterghem C, Moraga-Cid G, *et al* (2013) Structural basis for ion permeation mechanism in pentameric ligand-gated ion channels. EMBO J 32(5):728–741.
9. Hilf RJ, Dutzler R (2009) Structure of a potentially open state of a proton-activated pentameric ligand-gated ion channel. Nature 457(7225):115–118.
10. Prevost MS, Sauguet L, Nury H, Van Renterghem C, Huon C, *et al* (2012) A locally closed conformation of a bacterial pentameric proton-gated ion channel. Nat Struct Mol Biol 19(6):642-649.
11. Gonzalez-Gutierrez G, Cuello LG, Nair SK, Grosman C (2013) Gating of the proton-gated ion channel from Gloeobacter violaceus at pH 4 as revealed by X-ray crystallography. Proc Natl Acad Sci U S A 110(46):18716-18721.
12. Althoff T, Hibbs RE, Banerjee S, Gouaux E (2014) X-ray structures of GluCl in apo states reveal a gating mechanism of Cys-loop receptors. Nature. 512(7514):333-7.

13. Hibbs RE, Gouaux E (2011) Principles of activation and permeation in an anion-selective Cys-loop receptor. Nature 474(7349):54–60.
14. Miller PS, Aricescu AR (2014) Crystal structure of a human $GABA_A$ receptor. Nature 512(7514):270-5.
15. Hassaine G, Deluz C, Grasso L, Wyss R, Tol MB, *et al* (2014) X-ray structure of the mouse serotonin 5-HT3 receptor. Nature 512(7514):276-81.
16. Duret G, Van Renterghem C, Weng Y, Prevost M, Moraga-Cid G, Huon C, Sonner JM, Corringer PJ (2011) Functional prokaryotic-eukaryotic chimera from the pentameric ligand-gated ion channel family. Proc Nat Acad Sci U S A 108(29):12143–12148.
17. Bocquet N, Prado de Carvalho L, Cartaud J, Neyton J, Le Poupon C, *et al* (2007) A prokaryotic proton-gated ion channel from the nicotinic acetylcholine receptor family. Nature 445(7123):116–119.
18. Grutter T, de Carvalho LP, Dufresne V, Taly A, Edelstein SJ, Changeux JP (2005) Molecular tuning of fast gating in pentameric ligand-gated ion channels. Proc Nat Acad Sci U S A 102(50):18207-18212.
19. Smart TG, Paoletti P (2012) Synaptic neurotransmitter-gated receptors. Cold Spring Harb Perspect Biol 4:(3)
20. Rajendra S, Lynch JW, Pierce KD, French CR, Barry PH, Schofield PR (1994) Startle disease mutations reduce the agonist sensitivity of the human inhibitory glycine receptor. J Biol Chem 269(29):18739–18742.
21. Rajendra S, Lynch JW, Pierce KD, French CR, Barry PH, Schofield PR (1995) Mutation of an arginine residue in the human glycine receptor transforms beta-alanine and taurine from agonists into competitive antagonists. Neuron 14(1):169–175.
22. Bode A, Lynch JW (2013) Analysis of hyperekplexia mutations identifies transmembrane domain rearrangements that mediate glycine receptor activation. J Biol Chem 288(47):33760–33771.
23. Bode A, Wood SE, Mullins JG, Keramidas A, Cushion TD, et al. (2013). New hyperekplexia mutations provide insight into glycine receptor assembly, trafficking, and activation mechanisms. J Biol Chem 288(47):33745–33759.
24. Lynch JW, Rajendra S, Pierce KD, Handford CA, Barry PH, *et al* (1997) Identification of intracellular and extracellular domains mediating signal

transduction in the inhibitory glycine receptor chloride channel. EMBO J 16:110–120.

25. Lape R, Plested AJR, Moroni M, Colquhoun D, Sivilotti LG (2012) The α1K276E startle disease mutation reveals multiple intermediate states in the gating of glycine receptors. J Neurosci 32(5):1336-52.
26. Saul B, Kuner T, Sobetzko D, Brune W, Hanefeld F, *et al* (1999) Novel GLRA1 missense mutation (P250T) in dominant hyperekplexia defines an intracellular determinant of glycine receptor channel gating. J Neurosci 19(3):869–877.
27. Bormann J, Rundström N, Betz H, Langosch D (1993) Residues within transmembrane segment M2 determine chloride conductance of glycine receptor homo- and hetero-oligomers. EMBO J 12(10):3729-37.
28. Eiselé JL, Bertrand S, Galzi JL, Devillers-Thiéry A, Changeux JP, *et al* (1993) Chimaeric nicotinic-serotonergic receptor combines distinct ligand binding and channel specificities. Nature 366(6454):479-483.
29. Bouzat C, Gumilar F, Spitzmaul G, Wang HL, Rayes D, *et al* (2004) Coupling of agonist binding to channel gating in an ACh-binding protein linked to an ion channel. Nature 430(7002):896-900.
30. Tillman TS, Seyoum E, Mowrey DD, Xu Y, Tang P (2014) ELIC-α7nAChR Chimeras Reveal a Prominent Role of the Extracellular-Transmembrane Domain Interface in Allosteric Modulation. J Biol Chem 289(20):13851-7.
31. Nury H, Bocquet N, Le Poupon C, Raynal B, Haouz A, *et al* (2010) Crystal structure of the extracellular domain of a bacterial ligand-gated ion channel. J Mol Biol 395(5):1114-27.
32. Mowrey DD, Cui T, Jia Y, Ma D, Makhov AM, *et al* (2013) Open-channel structures of the human glycine receptor α1 full-length transmembrane domain. Structure 21(10):1897-1904.
33. Dellisanti CD, Yao Y, Stroud JC, Wang ZZ, Chen L (2007) Crystal structure of the extracellular domain of nAChR alpha1 bound to alpha-bungarotoxin at 1.94 A resolution. Nat Neurosci 10(8):953-962.
34. Bondarenko V, Mowrey DD, Tillman TS, Seyoum E, Xu Y, *et al* (2014) NMR structures of the human α_7 nAChR transmembrane domain and associated anesthetic binding sites. Biochim Biophys Acta 1838(5):1389-1395.

35. Lobo IA, Trudell JR, Harris RA (2004) Cross-linking of glycine receptor transmembrane segments two and three alters coupling of ligand binding with channel opening. J Neurochem 90(4):962–969.
36. Mihic SJ, Ye Q, Wick MJ, Koltchine VV, Krasowski MD, et al (1997) Sites of alcohol and volatile anaesthetic action on GABA(A) and glycine receptors. Nature 389(6649): 385–389.

Figure Legends

Figure 1: Overall view of the Lily X-ray structure. (A) Side view of Lily. One chain is represented in cartoon with the ECD colored in blue, M1 in cyan, M2 and loop M2-M3 in orange, M3 and M4 in gray. **(B)** Scheme of the Lily construct with local modifications indicated. The sequence shows the M1 and M2 region, with the mutated residues in red. **(C)** Upper view of Lily with the same color code. **(D)** Typical pH-elicited current traces of Lily-His and GLIC-His expressed in S2 cells, and Lily-HA expressed in BHK cells. In this and all subsequent figures, horizontal bars indicate the duration of the proton applications with concentrations given as pH units.

Figure 2: Structure of the TMD of a Lily subunit

(A) Cα trace of a TMD monomer of Lily. The blue mesh is the 2mFo-DFc NCS-averaged electron density map contoured at a level of 1.5 σ. **(B)** Same representation as in (A) colored by residue B-factor according to scale shown. **(C)** Superimposition of the Cα trace of a TMD monomer of Lily (orange) and of GLIC-LC (green). **(D)** Enlarged representation of the tip of adjacent M2 helices of Lily with protein atoms in sticks. The blue mesh is the 2mFo-DFc NCS-averaged electron density map as defined in (A).

Figure 3: Ion channel architecture and interaction networks in Lily and GLIC-LC.

(A) Cartoon representation of the pore lined by M2 helices for GLIC-LC (left) and Lily (right). The two front helices were removed. Residues lining the pore are shown in stick. Radiating dashes show side chain hydrophobic interactions that plug the pore. The center panel shows the pore radius along the z axis, computed on the full atom model of GLIC-LC (green), GLIC-pH4 (black), GLIC-pH7 (gray), Lily (orange) and GluCl-Apo (blue). **(B)** Cartoon representation of the interaction network around the M2-M3 loop in GLIC-LC (left panel) and Lily X-ray structure (right panel). M2 and the M2-M3 loop of one subunit is colored orange, loop 7 from the same subunit colored blue. M1 and M2 helices from the adjacent subunit (n+1) are colored cyan. Radiating dashes represent interactions that are discussed in the text. The center panel shows the orientation of the view by the addition of the three remaining M2 helices that form the pore.

Figure 4: Phenotypes of the Q226E, Q266E, R271Q, K276C and V280M mutants on Lily

(A) Cartoon representation of a Lily subunit with the Cα of mutated residues shown in sphere. **(B)** Normalized dose-response curves in the whole cell configuration. Lower traces show single-channel recording (-60 mV and pH 6.0) of outside-out patches for WT and R271Q. **(C)** Sample trace for Q226E mutant showing the leak current observed at pH 8.0, the proton-elicited current and the inhibition of the leak current by 100 µM picrotoxin (PTX, quantified in the bar graph where error bars represent +/- SD). Lower panel shows single-channel recording (-60 mV and pH 8.0) of out-side out patches of Q226E. **(D)** Dose-response curves recorded in the whole cell configuration. **(E)** Dose-response curves recorded in whole cell configuration. **(F)** Single-channel recording (-60 mV and pH 8.0) of out-side out patches for the V280M mutant.

Figure 5: Phenotypes of the P250T and G254A mutants on Lily

(A) Sample trace for WT and P250T. **(B)** Normalized glycine dose-response relationships. **(C)** Typical traces (left) and corresponding bar graph (error bars as +/- SD) showing the percentage of current remaining after 1 s application of a pH4 solution. **(D,E)** single channel amplitudes of G254A at different potentials (pH 6.0). **(F)** Sample traces of G254A. Kinetics of currents onset were fitted with a monoexponential (bar graph, error bars are +/- SD).

Figure 6: Proposed gating mechanism of the TMD of the α_1GlyR

(A) Cartoon representation of the X-ray closed structure of Lily in upper and side views. In the side view, the two front subunits were removed. The M2 and M2-M3 loop of a single subunit are colored orange, its two adjacent M2s are colored pale orange, and the neighboring M1 from the adjacent subunit is colored cyan. **(B,C,D)** Enlarged view of the structure of Lily with the same color code and selected side chains shown in sticks. **(E,F,G,H)** Same representation than in (A-D) of the open-pore homology model of Lily based on GLIC-pH4, with M2s and the M2-M3 loop colored yellow. **(D,G)** Closed and open models of Lily with an EtOH molecule in pink sphere positioned as in the GLIC(F238A)-EtOH co-crystal structure, and which overlaps with the EtOH potentiating binding site of the α_1GlyR. Note that in the open

model EtOH would elicit multiple stabilizing interactions with neighboring residues as shown by dashes, while no such interactions are observed in the closed form.

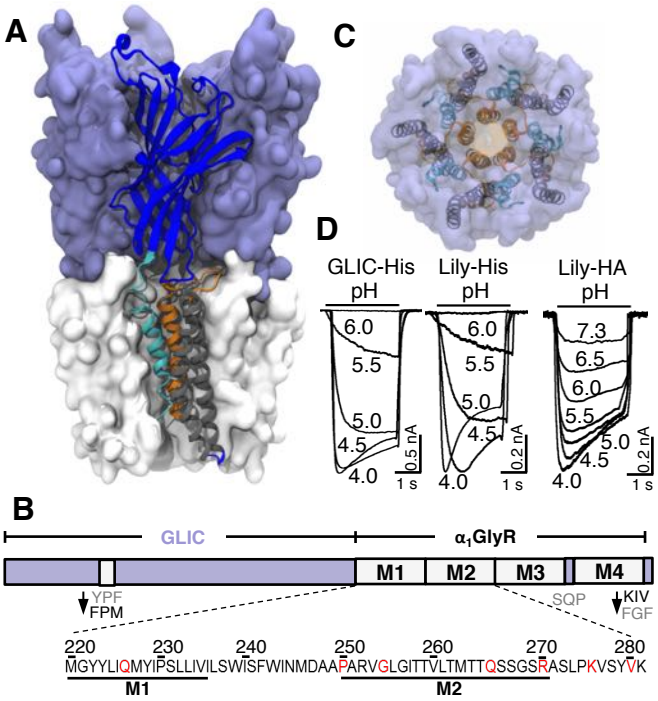
A
C
D
GLIC-His
pH
Lily-His
pH
Lily-HA
pH
6.0
5.5
5.0
4.5
4.0
7.3
6.5
6.0
5.5
5.0
4.5
4.0
0.5 nA
0.2 nA
0.2 nA
1 s
1 s
1 s
B
GLIC
α1GlyR
M1
M2
M3
M4
YPF
FPM
SQP
KIV
FGF
220
230
240
250
260
270
280
MGYYLIQMYIPSLLIVILSWVSFWINMDAAPARVGLGITTVLTMTTQSSGSRASLPKVSYVK
M1
M2

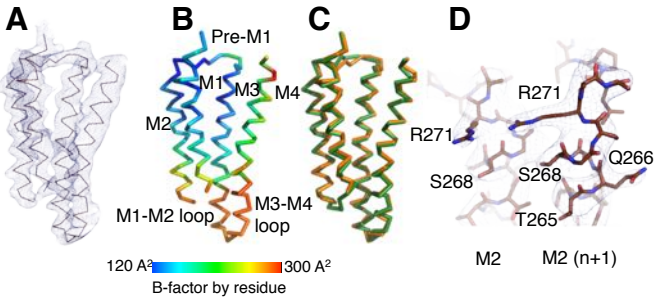
A
B
C
D
Pre-M1
M1
M3
M4
M2
M1-M2 loop
M3-M4 loop
120 A²
300 A²
B-factor by residue
R271
R271
Q266
S268
S268
T265
M2
M2 (n+1)

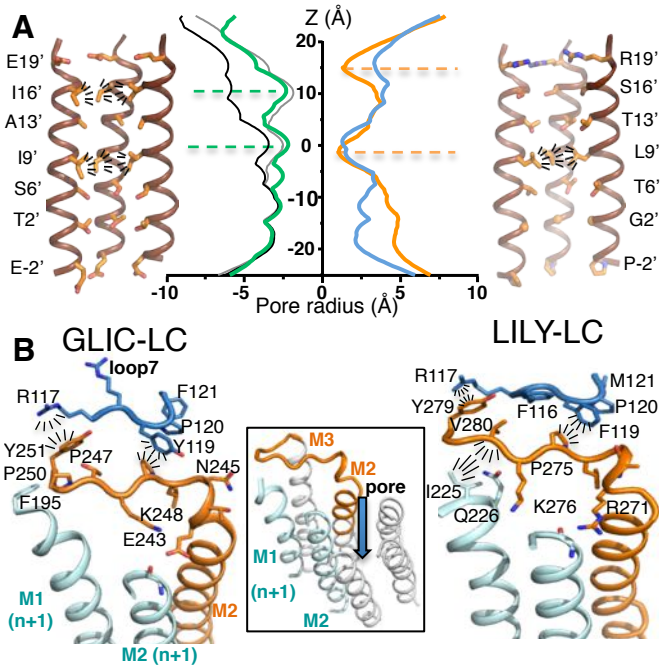
A
E19'
I16'
A13'
I9'
S6'
T2'
E-2'
Z (Å)
20
10
0
-10
-20
-10
-5
0
5
10
Pore radius (Å)
R19'
S16'
T13'
L9'
T6'
G2'
P-2'
B
GLIC-LC
loop7
R117
F121
P120
Y119
Y251
P247
P250
N245
F195
K248
E243
M1
(n+1)
M2
M2 (n+1)
M3
M2
pore
M1
(n+1)
M2
LILY-LC
R117
M121
Y279
F116
P120
V280
F119
P275
I225
Q226
K276
R271

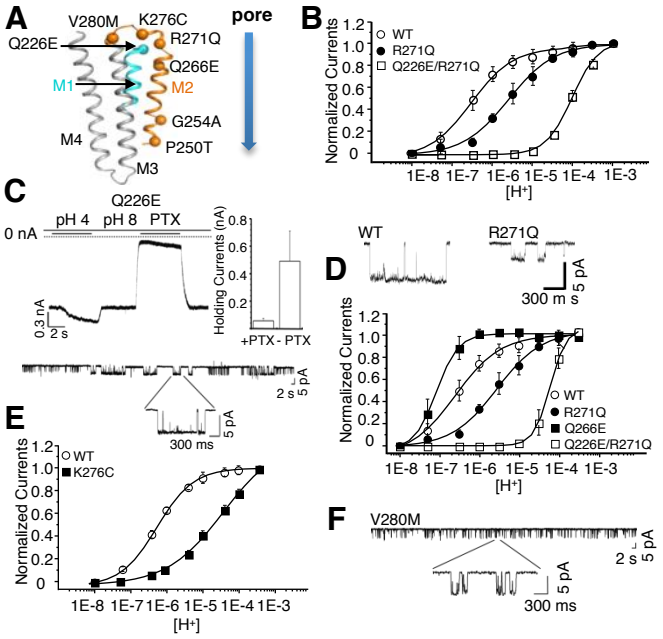
A
V280M
K276C
Q226E
R271Q
Q266E
M1
M2
G254A
M4
P250T
M3
pore
B
WT
R271Q
Q226E/R271Q
Normalized Currents
[H+]
C
Q226E
pH 4
pH 8
PTX
0 nA
0.3 nA
2 s
Holding Currents (nA)
+PTX - PTX
2 s
5 pA
300 ms
D
WT
R271Q
5 pA
300 m s
Q266E
E
K276C
F
V280M

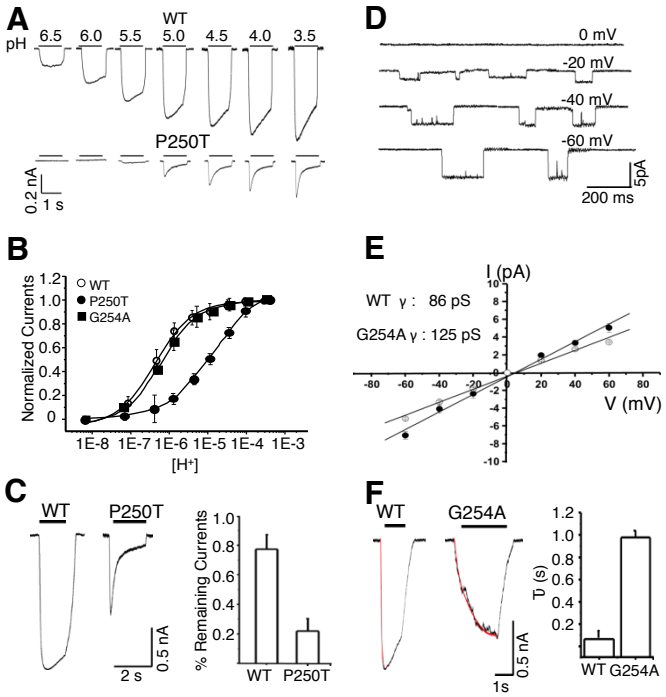
A
pH
6.5
6.0
5.5
WT
5.0
4.5
4.0
3.5
P250T
0.2 nA
1 s
D
0 mV
-20 mV
-40 mV
-60 mV
5pA
200 ms
B
Normalized Currents
WT
P250T
G254A
1E-8 1E-7 1E-6 1E-5 1E-4 1E-3
[H+]
E
I (pA)
WT γ : 86 pS
G254A γ : 125 pS
V (mV)
C
WT
P250T
0.5 nA
2 s
% Remaining Currents
WT P250T
F
WT
G254A
0.5 nA
1s
τ (s)
WT G254A

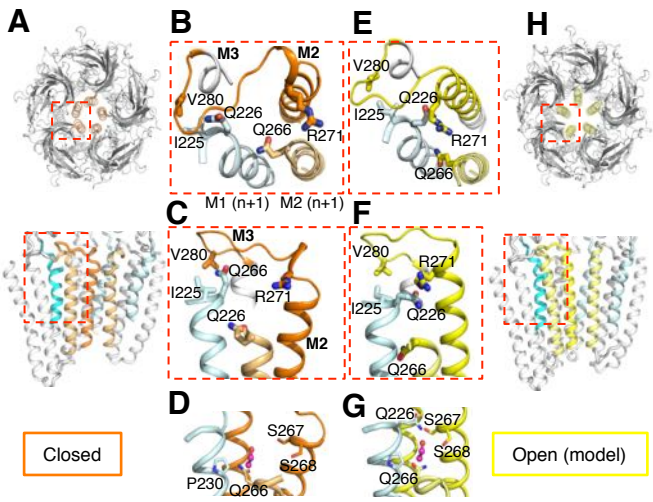
A
B
E
H
M3
M2
V280
Q226
Q266
R271
I225
M1 (n+1)
M2 (n+1)
C
F
M3
V280
Q266
I225
R271
Q226
M2
V280
R271
I225
Q226
Q266
D
G
S267
S268
P230
Q266
Q226
S267
S268
Q266
Closed
Open (model)

Supporting Information.

Materials and Methods

Protein Production

The cDNA coding for Lily-His consists, from the N- to the C-terminus, in a Drosophilia signal peptide (MKLCILLAVVAFVGLSLG), the mature sequence of Lily followed to a C-terminal his-tag inserted into a pMT/BiP/V5-HisA vector (Invitrogen). This plasmid and the pPURO selection-plasmid (19 µg and 1 µg, respectively) were co-transfected into S2-type insect cells in the presence of cellfectin (Invitrogen). Co-transfected cell-lines were grown in Insect-XPRESS medium (Lonza) supplemented with 0.6 µg/ml puromycine at 28°C without CO_2. Cell-lines are considered stable after 3-4 weeks. Protein expression is induced upon addition of Cadmium (5 µM) when the culture reaches a cell-density population of 10^7 cells/ml. Cells were collected by centrifugation (1500 g for 10 minutes). Lily-His was extracted and purified following the same procedure as described previously (1). In brief, cells were broken by sonication at 4°C in Buffer A (Tris 20 mM, NaCl 300 mM). Membranes were recovered by centrifugation (1h at 40000 rpm) and solubilized using DDM 2% in Buffer A with agitation overnight at 4°C. The supernatant was collected by centrifugation at 20000 rpm (1h). Lily was finally recovered from the supernatant by affinity chromatography using Cobalt resin, eluted using imidazole (250 mM) and purified by size exclusion chromatography.

Crystallography

Crystal Preparation

All crystals were obtained using vapor diffusion in hanging drops at 20°C. The concentrated (6–8 mg/ml) protein was mixed in a 1:1 ratio with reservoir solution typically containing 16–20% PEG 2000MME, 50 mM $NiCl_2$, 4% DMSO, 11% ethylene glycol and 0.1 M NaAcetate pH 3.0. Crystallization was induced by the micro-seeding technique from a solution of crushed crystals 1 hour after setting-up the crystallization experiment. Crystals appeared overnight and grew for one week before reaching their final dimensions (typically 100 µm x 100 µm x 100 µm). All crystals were cryo-protected using a three-step protocol. 1) The crystal-containing drops were transferred to the cold room (4°C), sealed onto a novel crystal plate that contained no

reservoir solution and left at 4°C for 10 minutes. 2) 3-5 µl of a dehydrating solution composed of the reservoir solution supplemented with 30% of ethylene glycol was added to the crystallization drop. 3) The drop was left to air-dry for 5-20 minutes prior to flash-freezing in liquid nitrogen.

Data Collection

Datasets were collected on beamline ID23-1 of the European Synchrotron Radiation Facility (Grenoble, France). Crystals were collected using the helicoïdal data collection facility. Reflections were integrated using XDS(2) and further processed using the CCP4 programs (2). Crystals of Lily-His belong to the $P2_12_12_1$ space group (a,b,c=118.9, 132.3, 190.5Å and α=β=γ=90°) with one pentamer in the asymmetric unit. Details on the data collection statistics are provided in Table S1.

Phasing and Refinement

The molecular replacement solution was found in Phaser (3) by using the structure of GLIC (PDB 4HFI) at 2.4 Å as a starting model. This initial model was refined in Refmac 5 (4) by using rigid-body refinement and subsequently, by using restrained refinement (4). The resulting model was improved by manual building in COOT (5). The model was finally refined in Buster (6). Automatically-generated non-crystallographic symmetry restraints were thus used throughout refinement (7). Right after molecular replacement, B-factors were reset to an arbitrary value of 120 corresponding to the Wilson-plot estimated B-factors and set constant until the final steps of refinement. B-factors were then refined using 2 TLS parameter by chain (one for the ECD (residue 5 to 191), one for the TMD (residue 218 to 413)). NCS symmetry averaging improves the quality of the electron density thus allowing the unambiguous reconstruction of the main chain except for the first four N-terminal residues, the M1-M2 loop (residue 218-222) as well as the C-terminal 10-histidine expression tag. Model geometry validation: 94.8% of the residues were in the most favored regions of the Ramachandran plot. MolProbity scores (8) for the refined model ranged within the 100^{th} percentiles of structures refined at comparable resolutions. Details of the refinement statistics are provided in Table S1.

Homology Modelling

We constructed three homology models of Lily. The first model completes the missing parts of the crystal structure of Lily-His in the LC state. The others propose a model of Lily in the open state (based on GLIC-pH4) and the resting state (based on GLIC-pH7). We manually created the sequence alignment between GLIC and Lily, as it is straightforward since only one gap could be found in the M1-M2 loop.

For the LC structural model of Lily, we used as a template the presented crystal structure of Lily as well as parts of the crystal structure of GLIC in the same crystal packing (see below). The homology models were constructed while keeping all completely attributed residues, in the used Lily structure, as rigid body constraints, and thus not modified. To model the missing part of the M1-M2 loop we used the structure of four residues of GLIC in the M1-M2 loop (residues 218 to 221 [STST], ST—SY, see Figure 1) as a structural template. For the last of the five Lily chains, the last helix turn of M1 was missing, we used the same strategy as described previously, by adding the residues 213 to 216 (TAFW) from GLIC as structural template. For the open model of Lily, we used as a template the high-resolution structure of GLIC in the open state (PDB: 4HFI) (9). The whole ECD (residues 5 to 191) of GLIC was used as a rigid body constraint with the exception of the two loops in contact with the TMD, loop loop2 (residues 31 to 33) and loop7 (residues 112 to 122).

The Modeller software (10) was used to generate 100 homology models of each state. The best scoring model was chosen for the last step of side-chain refinement. All residue side chains which were not part of the rigid body restraints were rebuilt using the backbone-dependent rotamer library SCRWL4 (11). Radii were calculated using the program Hole (12)

Electrophysiology

cDNA Constructs.

The cDNA construct encoding the Lily receptors with a C-terminal HA-tag subcloned into the pMT3 vector for expression in BHK cells has been described previously (13). Mutations were inserted by using the QuikChange site-directed mutagenesis method. All constructions were confirmed by full sequencing.

Cell Culture and Transfection.

BHK cells tk-ts13 variant, display weak endogenous proton-gated currents and are therefore favorable to record Lily and its mutants. Cells were grown at 37 °C under a 5% CO_2 atmosphere in DMEM with Glutamax (Invitrogen), supplemented with 5% fetal bovine serum (FBS), penicillin (0.1 g/L), and streptomycin (100 U/mL). Cells were seeded at 104 cells/cm2 in 35-mm Petri dishes 24 h before transfection. Cells were transfected with 4µg of cDNA of interest and 1µg of GFP-cDNA cloned into the pMT3 vector using the calcium phosphate precipitation method, GFP-positive cells were used for electrophysiology 16-24h after transfection. For recordings performed in S2 cells, stable cell lines were grown in Insect-XPRESS medium supplemented with 0.6 µg/ml puromycine at 28°C without CO_2. 5 days before patch experiments, Lily expression was induced upon addition of Cadmium (5 µM). The day before, cells were plated in 35mm dishes coated with poly-L-lysine (Sigma-Aldrich).

Patch-Clamp Recordings.

Whole-cell recordings in BHK and S2 cells were performed using a holding potential of −60 mV. Patch electrodes were filled with (in mM): 140 CsCl, 2 MgCl2, 2 Ca2Cl, 10 BAPTA, 10 HEPES (pH 7.4). The external solution contained (in mM): 150 NaCl, 10 KCl, 2.0 CaCl2, 1.0 MgCl2, 10 HEPES (pH 7.4), and 10 glucose. The amplitude of currents was assayed using a brief (1–2 s) pulse with external solution at desired pHs every 60 seconds. Proton dose-response curves were calculated normalizing the maximal current at each proton concentration to the maximal current obtained at saturating concentrations of the protons (100%). EC_{50}, nH and τ_{act} values and plots were constructed using the Origin 6.0 (MicroCal) software. To calculate the coupling energy between pair of residues, mutant cycle analysis was performed as described previously (14) using the equation,

$$\Delta G = RT\ ln\begin{bmatrix} EC50, ww * EC50, mm \\ EC50, wm * EC50, mw \end{bmatrix}$$

where ΔG is the coupling energy, R is the universal gas constant, T is temperature (K), $EC_{50,ww}$ is the wild type EC_{50} value, $EC_{50,mm}$ is the double mutant EC_{50} value, and $EC5_{0,mw}$ and $EC_{50,wm}$ are the two single mutant EC_{50} values

The methodology for single-channel recordings in the outside-out configuration has been previously published (13). Briefly, patch pipettes had tip resistances of 7–15 megaohms following fire polishing. Patchs were voltage clamped at −60 mV and the data were filtered (5 kHz low-pass 8-pole Bessel) and acquired at 50 kHz using pClamp software (Molecular Devices, Sunnyvale, CA). The solutions at different pHs were applied to the patch using a gravity-driven solution exchanger perfusion system. Cells were maintained in extracellular medium containing (in mM): 150 NaCl, 10 KCl, 2.0 CaCl2, 1.0 MgCl2, 10 HEPES (pH 7.4), and 10 glucose. The intracellular recording solution contained (in mM): 140 CsCl, 2 MgCl2, 2 Ca2Cl, 10 BAPTA, 10 HEPES (pH 7.4). Conductance values were obtained from plots I/V constructed using the Origin 6.0 software.

References

1. Bocquet N, Nury H, Baaden M, Le Poupon C, Changeux JP, et al (2009) X-ray structure of a pentameric ligand-gated ion channel in an apparently open conformation. Nature 457 (7225):111–114.
2. CCP4 (1994) The CCP4 suite: programs for protein crystallography. Acta Crystallogr D Biol Crystallogr 50:760-763.
3. McCoy AJ, Grosse-Kunstleve RW, Adams PD, Winn MD, Storoni LC, *et al* (2007) Phaser crystallographic software. J Appl Crystallogr 40(Pt 4):658-674.
4. Murshudov GN, Vagin AA, Dodson EJ (1997) Refinement of macromolecular structures by the maximum-likelihood method. Acta Crystallogr D Biol Crystallogr 53(Pt 3):240-255.
5. Emsley P, Cowtan K (2004) Coot: model-building tools for molecular graphics. Acta Crystallogr D Biol Crystallogr 60(Pt 12 Pt 1):2126-2132.
6. Blanc E, Roversi P, Vonrhein C, Flensburg C, Lea SM, *et al* (2004) Refinement of severely incomplete structures with maximum likelihood in BUSTER-TNT. Acta Crystallogr D Biol Crystallogr 60(Pt 12 Pt 1):2210-2221.
7. Smart OS, Womack TO, Flensburg C, Keller P, Paciorek W, *et al* (2012) Exploiting structure similarity in refinement: automated NCS and target-structure restraints in BUSTER. (Translated from eng) Acta Crystallogr D Biol Crystallogr 68(Pt 4):368-380.

8. Davis IW, Leaver-Fay A, Chen VB, Block JN, Kapral GJ, *et al* (2007) MolProbity: all-atom contacts and structure validation for proteins and nucleic acids. (Translated from eng) Nucleic Acids Res 35(Web Server issue):W375-383.
9. Sauguet L, Shahsavar A, Poitevin F, Huon C, Menny A, *et al* (2014) Crystal structures of a pentameric ligand-gated ion channel provide a mechanism for activation. Proc Natl Acad Sci U S A 111(3):966-971.
10. Sali A, Blundell TL (1993) Comparative protein modelling by satisfaction of spatial restraints. J Mol Biol 234(3):779–815.
11. Krivov GG, Shapovalov MV, Dunbrack Jr. RL (2009) Improved prediction of protein side-chain conformations with SCWRL4. Proteins 77(4):778-795.
12. Smart OS, Goodfellow JM and Wallace BA. The Pore Dimensions of Gramicidin A. Biophysical Journal 65:2455-2460(1993)
13. Duret G, Van Renterghem C, Weng Y, Prevost M, Moraga-Cid G, *et al* (2011) Functional prokaryotic-eukaryotic chimera from the pentameric ligand-gated ion channel family. Proc Nat Acad Sci U S A 108(29):12143–12148.
14. Bode A, Lynch JW (2013) Analysis of hyperekplexia mutations identifies transmembrane domain rearrangements that mediate glycine receptor activation. J Biol Chem 288(47):33760–33771.
15. Mowrey DD, Cui T, Jia Y, Ma D, Makhov AM, *et al* (2013) Open-channel structures of the human glycine receptor α1 full-length transmembrane domain. Structure 21(10):1897-1904
16. Miller PS, Aricescu AR (2014) Crystal structure of a human GABAA receptor. Nature 512(7514):270-5.
17. Bond PJ, Sansom MS (2003) Membrane protein dynamics versus environment: simulations of OmpA in a micelle and in a bilayer. J Mol Biol 329(5):1035-53.
18. Canlas CG, Ma D, Tang P, Xu Y (2008) Residual dipolar coupling measurements of transmembrane proteins using aligned low-q bicelles and high-resolution magic angle spinning NMR spectroscopy. J Am Chem Soc 130(40):13294-13300.

Figures

Figure s1: Crystal packing of Lily. (A) Sequence alignment between GLIC (blue), Lily (blue and black) and α_1GlyR (black). Conserved residues are indicated in red characters meanwhile the mutated residues in lily are indicated in yellow**. (B)** P222 crystal packing of Lily and comparison with the **(C)** C2 packing obtained for GLIC-pH4**.**

Figure s2: Missing atoms in the Lily refined crystal structure. (A) Sequence-alignment of the five chains constituting the TMD of Lily. Residues are respectively colored in blue and red when the whole residue or its side chain has been omitted from the final model. **(B)** Cartoon representation of a TMD of Lily. Residues are colored in red when their side chains are missing in all five monomers and in pink when modeled at least one in monomer. **(C**) Thermostability of GLIC-His and Lily purified in detergent solution. The purified protein samples (500µL at 0.2 mg/mL) were incubated over a range of temperatures for 10 min using a thermal cycler, followed by centrifugation to remove precipitated material. The supernatant was then loaded onto a superose 6 column equilibrated with SEC buffer (20mM Tris pH 7,5, 300mM NaCl, 0,02% DDM) and run at the flow rate of 0,5mL/min. The eluent was detected by UV absorption at 280nm.

Lily thus displays marked flexibility at the level of M4 and at the cytoplasmic side of the TMD, a feature observed in the crystal and possibly related to the lower thermal stability of Lily versus GLIC observed in detergent solution. Such flexibility may have several origins: 1) it may be due to the lack of the intracellular domain, an ~88 amino acid segment between the M3 and M4 that is present in α_1GlyR but has been removed in Lily. However, it is noteworthy that in the GluCl structures, the bottom segment of the TMD is well ordered while the cytoplasmic domain was removed in a similar manner as in Lily; 2) specific lipids may be needed to constrain the TMD of the α_1GlyR, a feature well documented for nAChRs and 3) an interesting possibility would be that the α_1GlyR carries a TMD intrinsically flexible in its closed-channel conformation. This may be related to its TMD structure that carries a single ring of hydrophobic residues at position 261 that hold together the M2 helices in the closed channel, together with the presence of two rings of glycine residues at positions 254 and 256 that may confer backbone flexibility. Thus, the observed flexibility might be

an intrinsic property of the closed-channel conformation, a feature that might have functional implication for channel activation. Upon activation, a conformational change might stabilize the intracellular side of the TMD as well as the intracellular end of the pore that hosts the selectivity filter.

Figure s3: (A) Ion permeation pathway. Cartoon representations of the ion channel of Lily, ELIC (PDBid: 2VL0), GLIC Active (PDBid: 4HFI), GLIC Resting (PDBid: 4NPQ) and GluCl Apo (PDBid: 4TNV), with the 2 front helices removed. The green grids show the volume accessible to the solvent. Side chains of pore lining residues are shown as sticks. **(B) ECD-TMD interface in Lily and GLIC-LC.** Cartoon representation of the domain interface of a monomer of GLIC-LC and Lily with the ECD colored blue, the TMD colored white. Residues contributing to the interface are shown in sticks and colored according to their location and conservation between GLIC and Lily. At the ECD, conserved (vs non-conserved) residues are colored blue (vs magenta). At the TMD conserved (vs non-conserved) residues are colored orange (vs red).

Figure s4: Electrophysiological characterization of Lily and α_1GlyR mutants. (A) Typical current traces of whole cell recordings for Lily WT and R271Q and K276C mutants. **(B)** Typical current traces of whole cell recordings for the α_1GlyR (without tag) WT, and R271Q and K276C mutants. **(C)** Normalized dose-response curves for α_1GlyR WT and the indicated mutants. **(D)** Single-channel events recording at -60 mV and pH 6.0 of outside-out patches containing Lily WT or K276C mutant **(E)** The I/V relationship plots summarized the mean channel amplitude obtained at different voltages of Lily WT and R271Q and K276C mutant. **(F)** Typical current traces of whole cell recordings for Lily WT, and Q226E/R271Q double mutant. **(G)** Sample trace for α_1GlyR Q226E mutant showing the leak current observed without glycine, the maximal glycine-elicited current (1mM) and the inhibition of the leak current by 100 µM picrotoxin (PTX, quantified in the bar graph where error bars represent +/- SD).

Figure s5: Electrophysiological characterization of Lily and α1GlyR mutants. (A) Typical current traces of whole cell recordings for α_1GlyR WT, R271Q and Q226E/R271Q mutants performed at pH 7.3 **(B)** Typical current traces of whole cell recordings for α_1GlyR WT, R271Q and Q226E/R271Q mutants performed at pH 5.

BHK cells were maintained in bath solution at pH 7.3 and glycine application (0.01-30 mM) was performed at pH 5. Note that the change in pH profoundly changes the pattern of activation by protons for mutants R271Q and Q226E/R271Q. At pH 7.3, glycine dose-response curves are well fitted by the Hill equation, while at pH 5 dose-responses curves seem to contain two components: a “high affinity component” underlying weak activation at low concentration of glycine, and a “low affinity component” underlying strong activation at high concentration of glycine. In addition, pH seems to alter the shape of the currents. **(C)** Upper graph: Normalized dose-response curves for α_1GlyR WT (EC_{50} 44 ± 6 µM), R271Q (EC_{50} 20± 2.5 mM) and Q226E/R271Q (EC_{50} 3.1 ± 0.4 mM) recorded at pH 7.3; Lower graph: Normalized dose-response curves for α_1GlyR WT (EC_{50} 78 ± 7µM), R271Q (EC_{50} 57± 8 mM) and Q226E/R271Q (EC_{50} 49 ± 6 mM) recorded at pH 5. **(D)** Typical current traces of whole cell recordings for Lily WT, Q266E and Q266E/R271Q mutants **(E)** Typical current traces of whole cell recordings for α_1GlyR WT, Q266E and Q266E/R271Q mutants **(F)** Normalized dose-response curves for α_1GlyR WT and the indicated mutants

Figure s6: (A) Modular structure of Lily. Cartoon representation of the X-ray structure of Lily, of GLIC-ECD expressed alone, and of the TMD of the α_1GlyR expressed alone and solved by NMR. The β-strands of the ECD are colored blue, the α-helix of the TMD are colored white, and the loops pink. The loop 7, pre-M1 and Loop M2-M3 are colored respectively green, cyan and red. **(B) Comparison of the TMDs of Lily and $GABA_A$ X-ray structures with the α_1GlyR NMR models**. The TMDs of Lily, the Lily open model, the $GABA_AR$ (PDB: 4COF (15) and the α_1GlyR NMR models (PDB: 2M6I (16) are represented as orange, yellow, black and red tubes, respectively. Note that α_1GlyR structure has been solved using NMR, as a consequence 15 structures have been displayed. All structures have been aligned using Cα atoms coordinates of M1, M2, M3, M4 helix and M2M3 loop. Right panel displays the rsmd of all presented structure versus themselves. Two atoms selection have been used for this calculation; the first selection contains the first of the five chains Cα atoms coordinates of the four helix, and the second selection contains the five chains Cα atoms coordinates of the four helix. These models show marked difference between the α_1GlyR NMR models and the Lily TMD structure. Differences in the M3-M4 loop at the bottom are probably due to a different linker, which is longer

in the isolated TMD (REFGGGGFI sequence) than in Lily (SQP sequence). However the rest of the TMD is identical in sequence between both structures, and we observed marked differences in the relative orientations of the helices. In addition, the M2-M3 linker is partly folded in helix and highly dynamic in the NMR models while it is folded in an extended conformation in Lily. The secondary structure of the TMD is highly conserved in all X-ray structures solved so far. It is highly unlikely that the TMD of the α_1GlyR would fold in different manner. The difference of the isolated TMD structure may be due to: 1) a lack of structural constraints applied by the ECD, 2) a mobilizing effect of the micellar environment (17), and 3) the NMR data may be compatible with other structural models since, in particular, the set of Overhauser effect (NOE) connectivity and paramagnetic relaxation enhancement (PRE) restraints cannot be unambiguously assigned to inter- or intra subunit distances, and the initial model used to build the TMD was based on residual dipolar coupling (RDC) constraints on a peptide comprising only the M2 and M3 segments (18).

Figure s7: Closed channel conformation of Lily (modeled by homology using GLIC-pH7; PDBid: 4NPQ) and comparison with the GluCl-apo closed (4TNV) structure. The upper view of Lily (A, B) and GluCl (E,H) are represented in the same manner as in figure 6B,E. M2 of a single subunit is colored orange and the neighboring M1 and M2 from the adjacent subunit are colored cyan and pale orange, respectively. Side views of Lily **(C)** and GluCl **(F)**. Side chains of Q226, Q266, R271 and D284 residues in Lily (E) and the homologous Q219, N259, N264 and D277 in GluCl are shown in sticks.

A

```
                                B1                  B2                  B3
                5    10        20        30        40        50        60        70        80
GLIC            VSPPPPIADEPLTVNTGIYLIECYSLDDKAETFKVNAFLSLSWKDRRLAFDPVRS-GVRVKTYEPEAIWIPEIRFVNVENAR----D
LILY            VSPPPPIADEPLTVNTGIYLIECYSLDDKAETFKVNAFLSLSWKDRRLAFDPVRS-GVRVKTYEPEAIWIPEIRFVNVENAR----D
GLYRα1          RIRPNFK-GPPVNVSCNIFINSFGSIAETTMDYRVNIFLRQQWNDPRLAYNEYPDDSLDLDPSMLDSIWKPDLFFANEKGAHFHEIT
                   30        40        50        60        70        80        90        100       110

                B4                  B5                  Loop 7              B6                  B7        B8        B9
                90        100       110       120       130       140       150       160       170
GLIC            ADVVDISVSPDGTVQYLERFSARVLSPLDFRRYPFDSQTLHIYLIVRSVDTRNIVLAVDLEKV-GKNDDVFLTGWDIESFTAVVKPA
LILY            ADVVDISVSPDGTVQYLERFSARVLSPLDFRRFPMDSQTLHIYLIVRSVDTRNIVLAVDLEKV-GKNDDVFLTGWDIESFTAVVKPA
GLYRα1          TDNKLLRISRNGNVLYSIRITLTLACPMDLKNFPMDVQTCIMQLESFGYTMNDLIFEWQEQGAVQVADGLTLPQFILKEEKDL-RYC
                        120       130       140       150       160       170       180       190

                    B10                 M1                  M2
                180       190       200       210       220       230       240       250
GLIC            NFALEDRLESKLDYQLRISRQYFSYIPNIILPMLFILFISWTAFWST--SYEANVTLVVSTLIAHIAFNILVETNLPKTPYMTYTGA
LILY            NFALEDRLESKLDYQLRISRQMGYYLIQMYIPSLLIVILSWISFWINMDAAPARVGLGITTVLTMTTQSSGSRASLPKVSYVKAIDI
GLYRα1          TKHYNTGKFTCIEARFHLERQMGYYLIQMYIPSLLIVILSWISFWINMDAAPARVGLGITTVLTMTTQSSGSRASLPKVSYVKAIDI
                200       210       220       230       240       250       260       270       280

                M3                  M4
                260       270       280       290       300       310
GLIC            IIFMIYLFYFVAVIEVTVQHYLKVESQPARAASITRASRIAFPVVFLLANIILAFLFFGF (GGHHHHHHHHHH)
LILY            WMAVCLLFVFSALLEYAAVNFVSRQSQPQRAKKIDKISRIGFPMAFLIFNMFYWIIYFGF (GGHHHHHHHHHH)
GLYRα1          WMAVCLLFVFSALLEYAAVNFVSRQ/-/QRAKKIDKISRIGFPMAFLIFNMFYWIIYKIVRREDVHNQ
                290       300       310       390       400       410       420
```

B

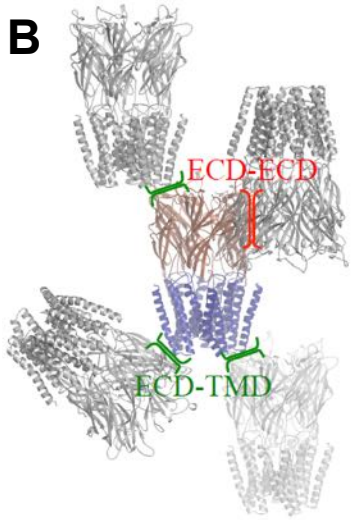

$P2_12_12_1$-type packing

C

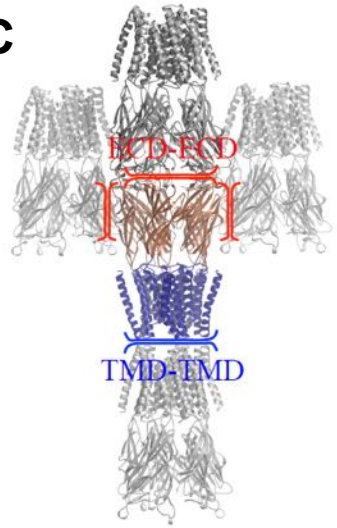

C2-type packing

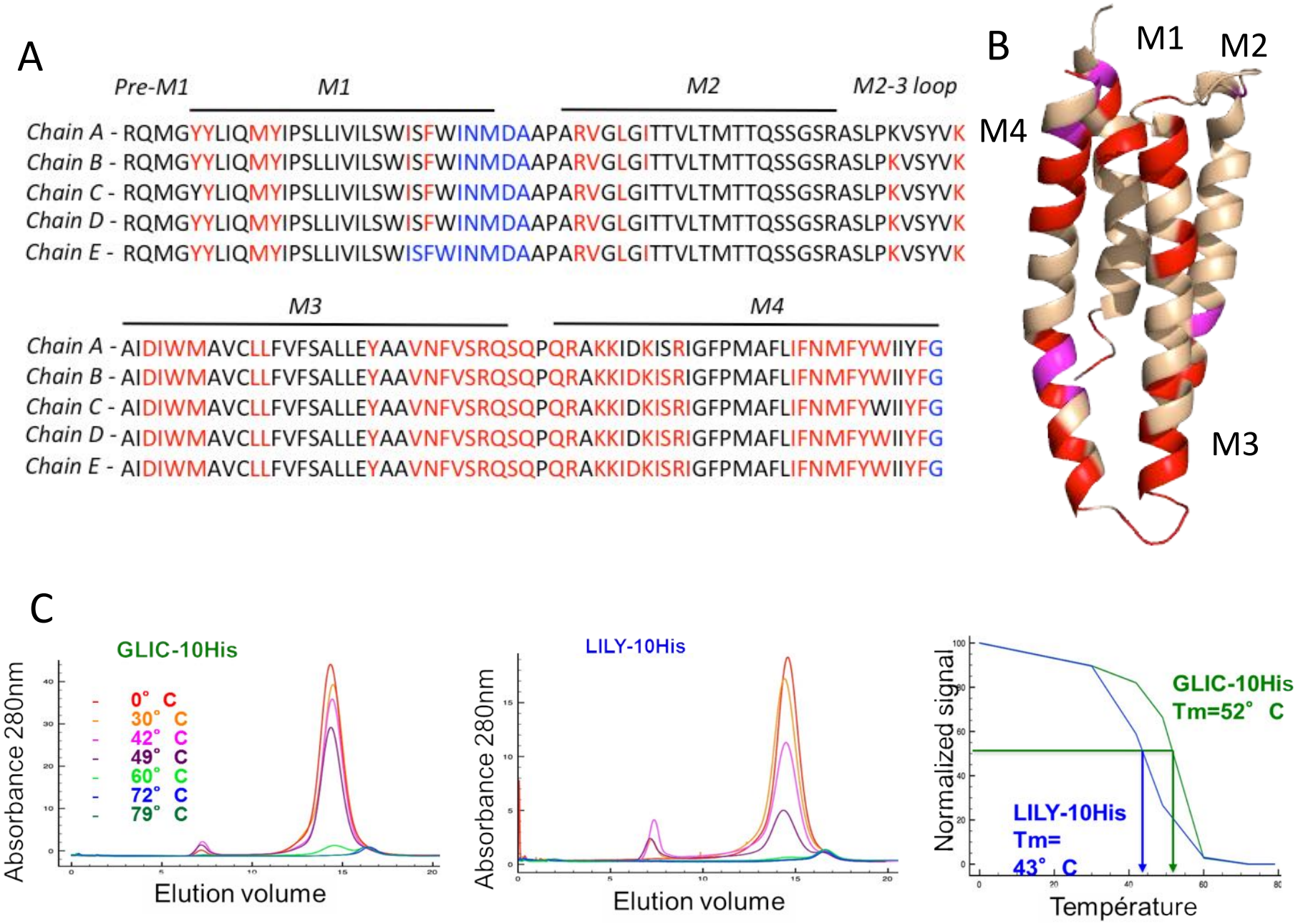
A
Pre-M1
M1
M2
M2-3 loop
Chain A - RQMGYYLIQMYIPSLLIVILSWISFWINMDAAPARVGLGITTVLTMTTQSSGSRASLPKVSYVK
Chain B - RQMGYYLIQMYIPSLLIVILSWISFWINMDAAPARVGLGITTVLTMTTQSSGSRASLPKVSYVK
Chain C - RQMGYYLIQMYIPSLLIVILSWISFWINMDAAPARVGLGITTVLTMTTQSSGSRASLPKVSYVK
Chain D - RQMGYYLIQMYIPSLLIVILSWISFWINMDAAPARVGLGITTVLTMTTQSSGSRASLPKVSYVK
Chain E - RQMGYYLIQMYIPSLLIVILSWISFWINMDAAPARVGLGITTVLTMTTQSSGSRASLPKVSYVK
M3
M4
Chain A - AIDIWMAVCLLFVFSALLEYAAVNFVSRQSQPQRAKKIDKISRIGFPMAFLIFNMFYWIIYFG
Chain B - AIDIWMAVCLLFVFSALLEYAAVNFVSRQSQPQRAKKIDKISRIGFPMAFLIFNMFYWIIYFG
Chain C - AIDIWMAVCLLFVFSALLEYAAVNFVSRQSQPQRAKKIDKISRIGFPMAFLIFNMFYWIIYFG
Chain D - AIDIWMAVCLLFVFSALLEYAAVNFVSRQSQPQRAKKIDKISRIGFPMAFLIFNMFYWIIYFG
Chain E - AIDIWMAVCLLFVFSALLEYAAVNFVSRQSQPQRAKKIDKISRIGFPMAFLIFNMFYWIIYFG
B
M1
M2
M4
M3
C
GLIC-10His
Absorbance 280nm
Elution volume
0° C
30° C
42° C
49° C
60° C
72° C
79° C
LILY-10His
Absorbance 280nm
Elution volume
Normalized signal
Température
GLIC-10His
Tm=52° C
LILY-10His
Tm=
43° C

A

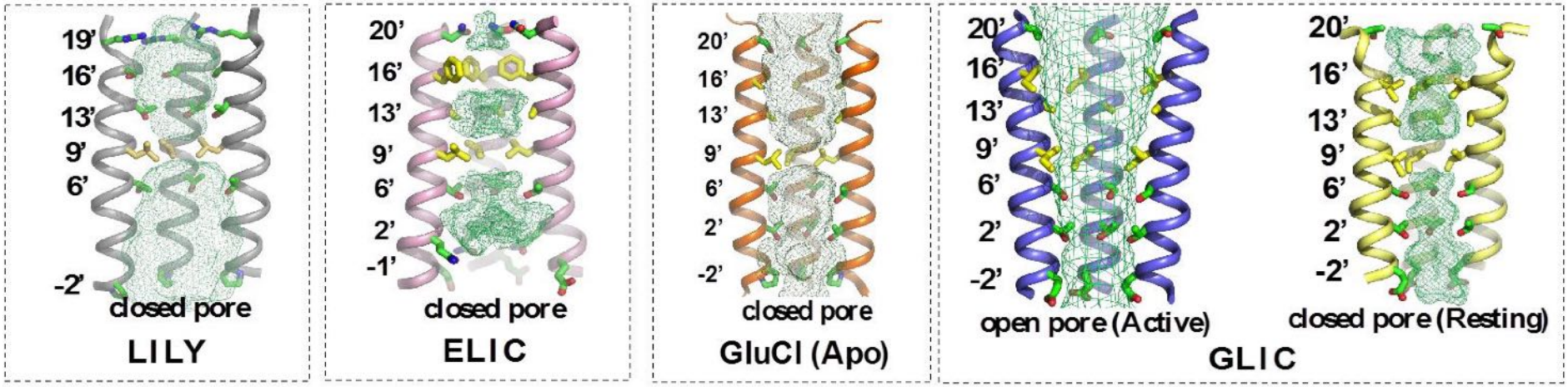
19'
16'
13'
9'
6'
-2'
closed pore
LILY
20'
16'
13'
9'
6'
2'
-1'
closed pore
ELIC
20'
16'
13'
9'
6'
2'
-2'
closed pore
GluCl (Apo)
20'
16'
13'
9'
6'
2'
-2'
open pore (Active)
20'
16'
13'
9'
6'
2'
-2'
closed pore (Resting)
GLIC

B

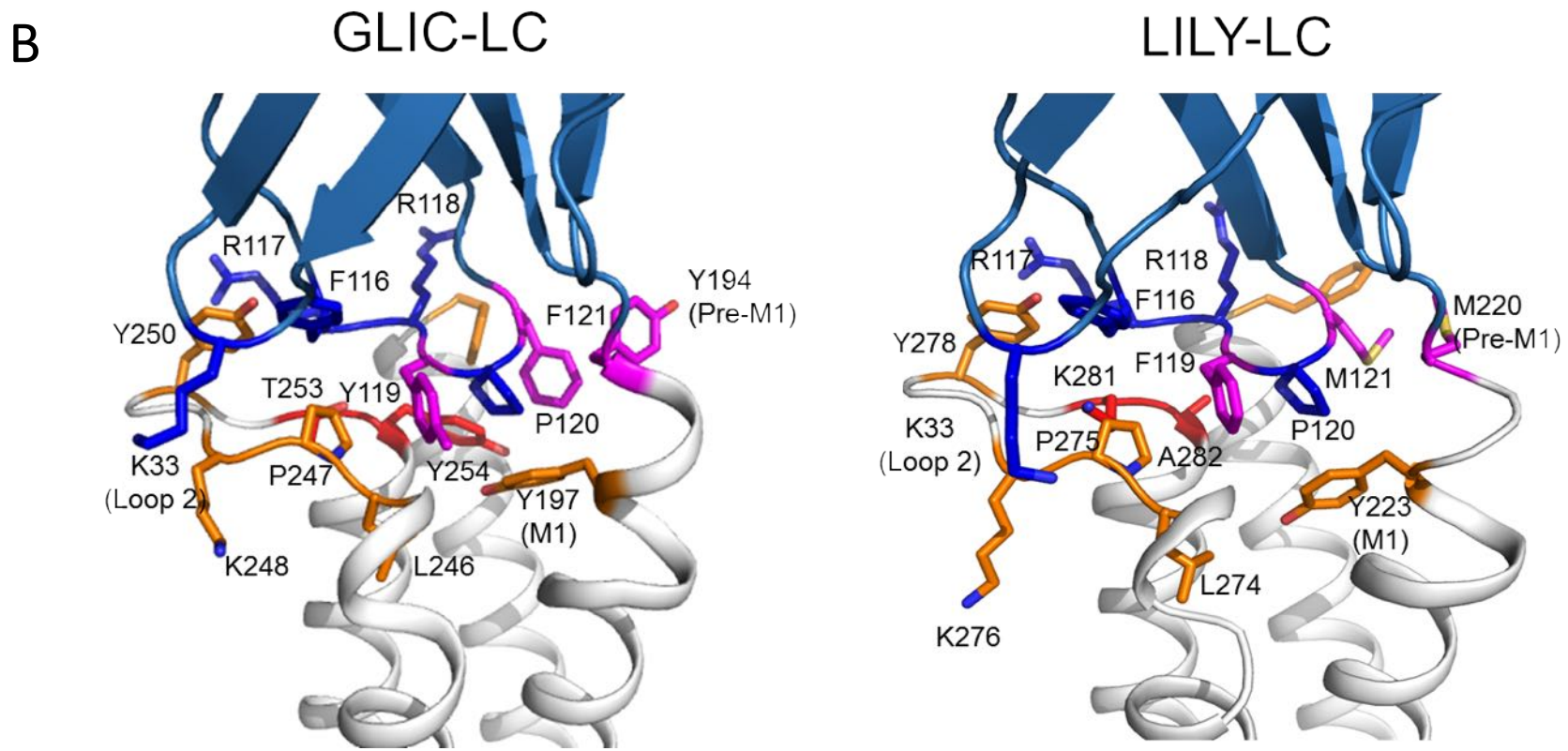
GLIC-LC
R118
R117
F116
Y194
(Pre-M1)
F121
Y250
T253
Y119
P120
K33
(Loop 2)
P247
Y254
Y197
(M1)
K248
L246
LILY-LC
R117
R118
F116
M220
(Pre-M1)
Y278
K281
F119
M121
K33
(Loop 2)
P275
A282
P120
Y223
(M1)
L274
K276

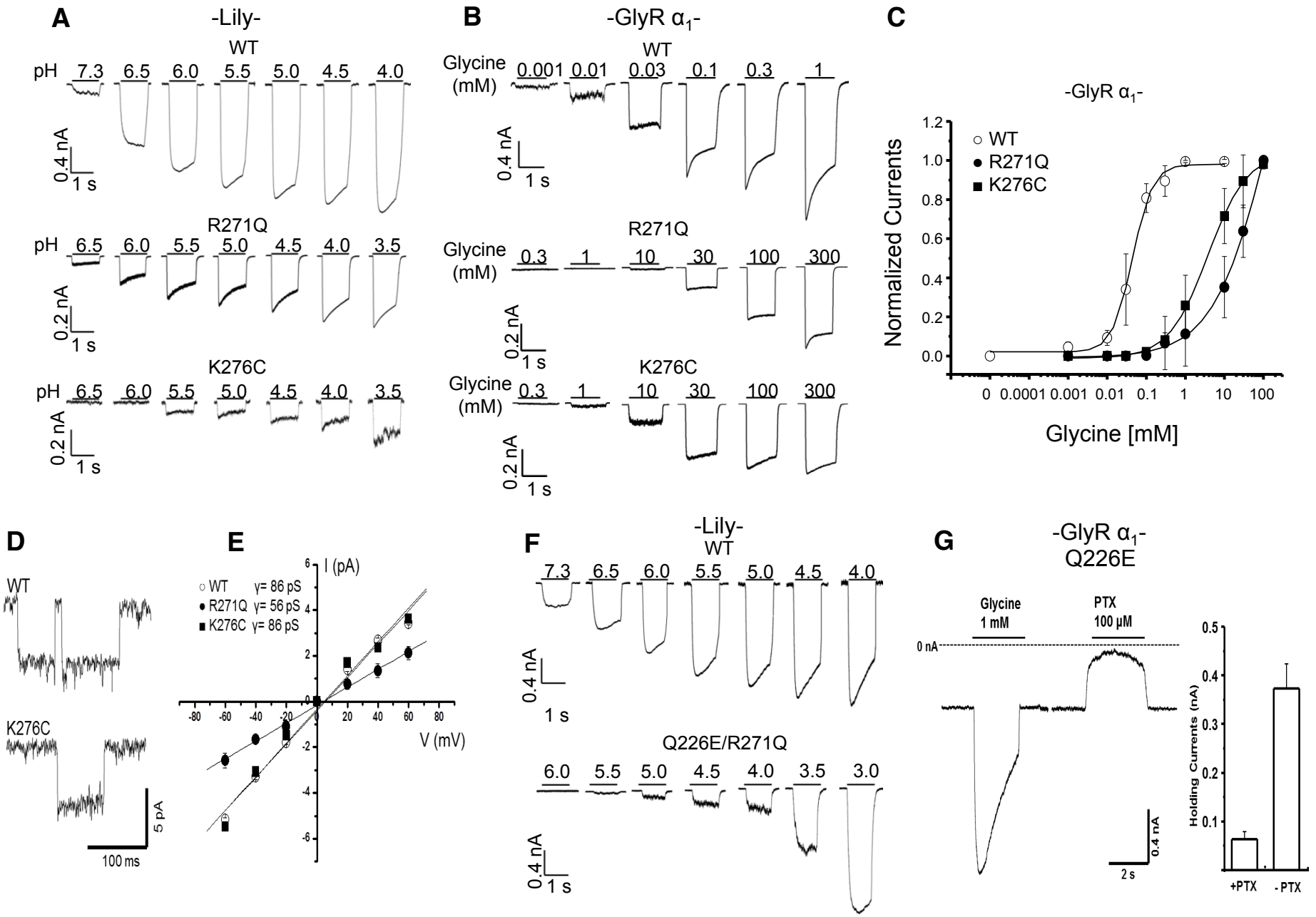
A
-Lily-
WT
pH 7.3 6.5 6.0 5.5 5.0 4.5 4.0
0.4 nA
1 s
R271Q
pH 6.5 6.0 5.5 5.0 4.5 4.0 3.5
0.2 nA
1 s
K276C
pH 6.5 6.0 5.5 5.0 4.5 4.0 3.5
0.2 nA
1 s
B
-GlyR α1-
WT
Glycine (mM) 0.001 0.01 0.03 0.1 0.3 1
0.4 nA
1 s
R271Q
Glycine (mM) 0.3 1 10 30 100 300
0.2 nA
1 s
K276C
Glycine (mM) 0.3 1 10 30 100 300
0.2 nA
1 s
C
-GlyR α1-
WT
R271Q
K276C
Normalized Currents
1.2
1.0
0.8
0.6
0.4
0.2
0.0
0 0.0001 0.001 0.01 0.1 1 10 100
Glycine [mM]
D
WT
K276C
5 pA
100 ms
E
I (pA)
WT γ= 86 pS
R271Q γ= 56 pS
K276C γ= 86 pS
V (mV)
F
-Lily-
WT
7.3 6.5 6.0 5.5 5.0 4.5 4.0
0.4 nA
1 s
Q226E/R271Q
6.0 5.5 5.0 4.5 4.0 3.5 3.0
0.4 nA
1 s
G
-GlyR α1-
Q226E
Glycine 1 mM
PTX 100 µM
0 nA
0.4 nA
2 s
Holding Currents (nA)
+PTX
- PTX

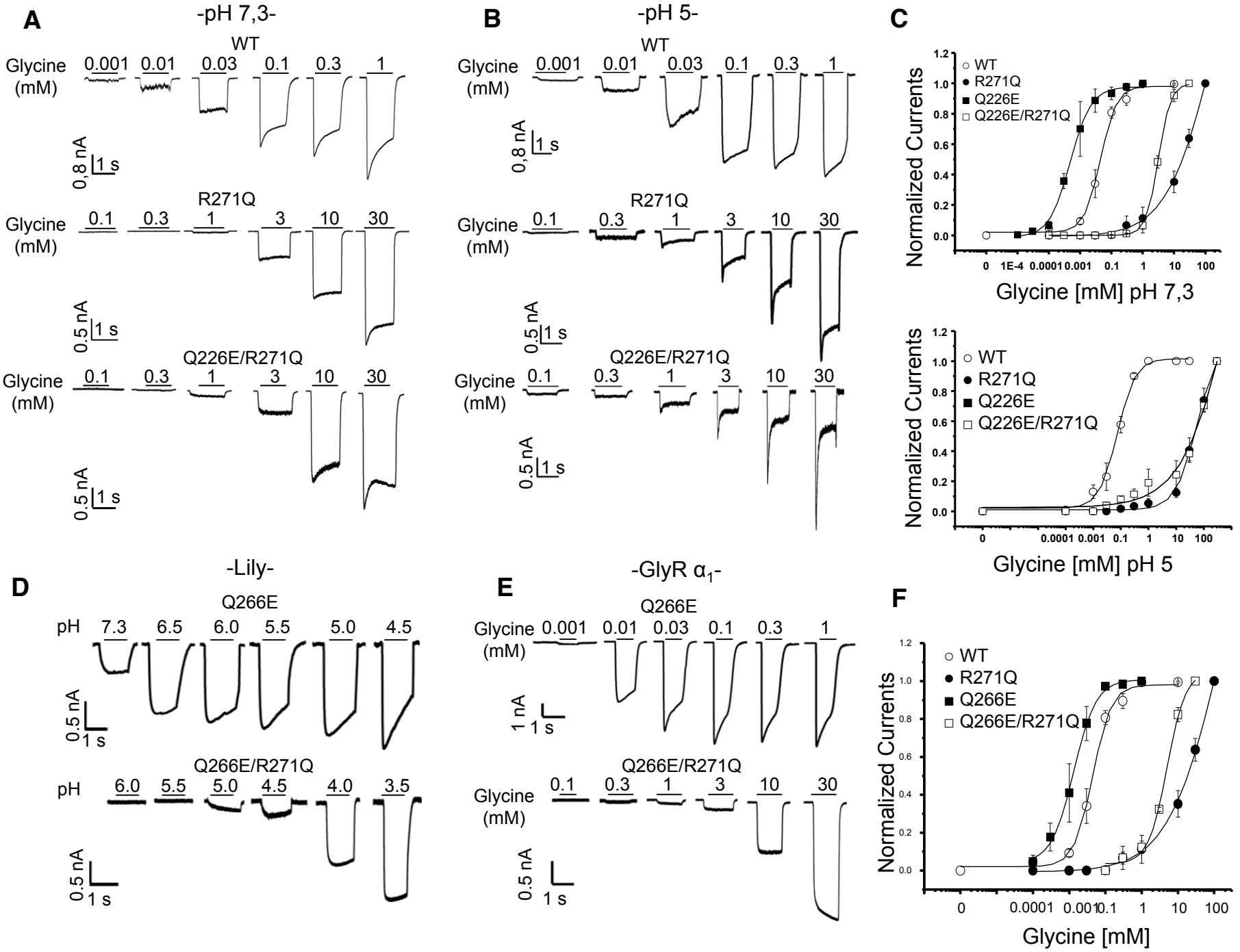
A
-pH 7,3-
WT
Glycine (mM)
0.001
0.01
0.03
0.1
0.3
1
0,8 nA
1 s
R271Q
0.1
0.3
1
3
10
30
0.5 nA
Q226E/R271Q
B
-pH 5-
C
Normalized Currents
WT
R271Q
Q226E
Q226E/R271Q
Glycine [mM] pH 7,3
Glycine [mM] pH 5
D
-Lily-
Q266E
pH
7.3
6.5
6.0
5.5
5.0
4.5
Q266E/R271Q
6.0
5.5
5.0
4.5
4.0
3.5
E
-GlyR α1-
1 nA
F
Q266E
Q266E/R271Q
Glycine [mM]

A

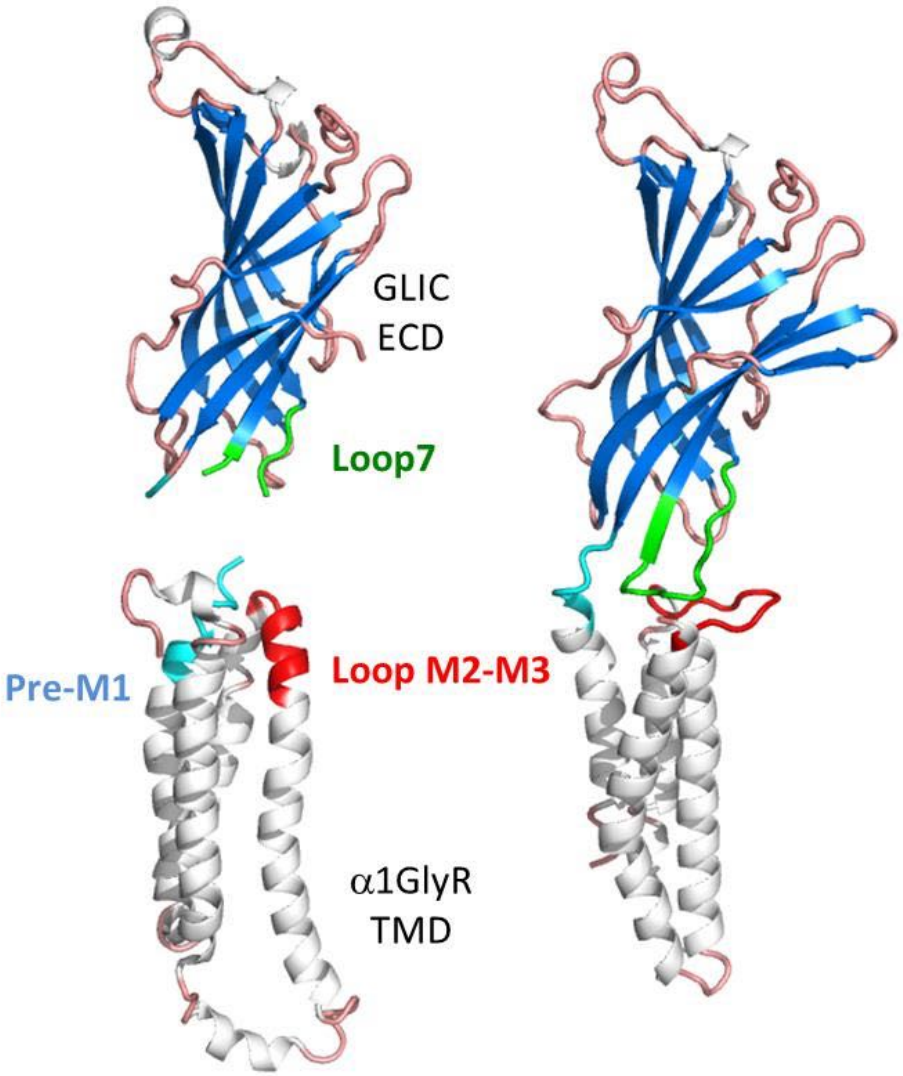

B

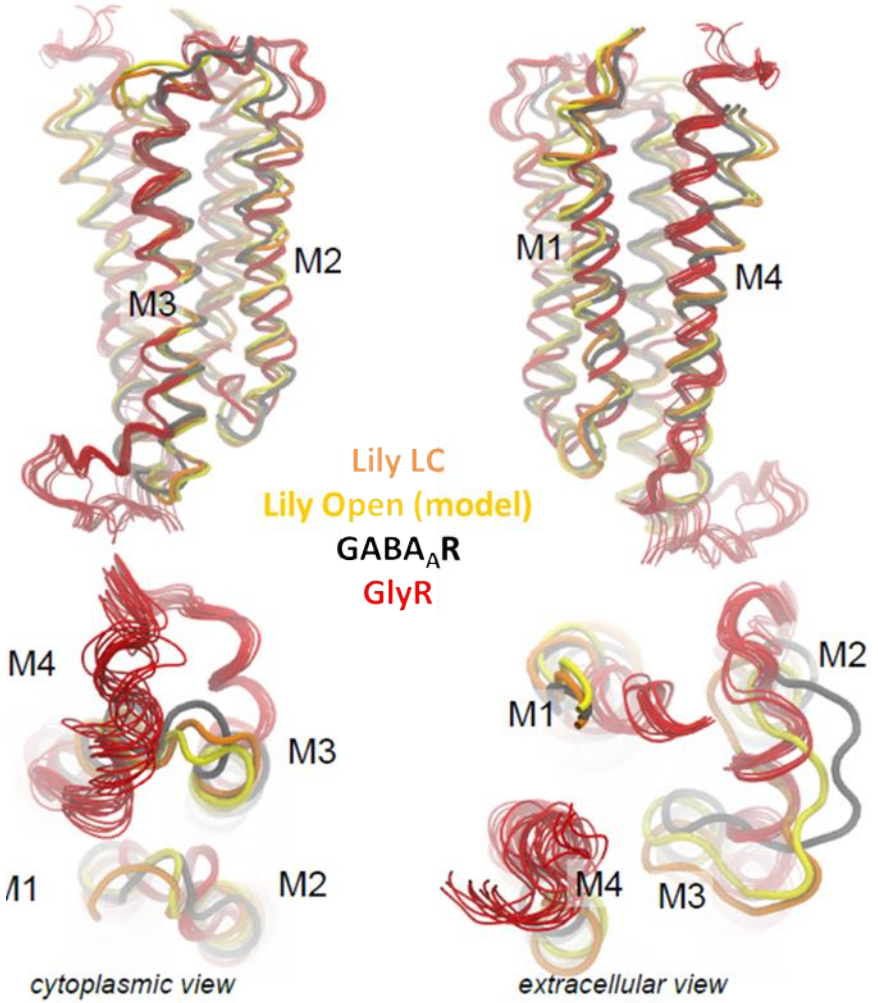

ased on Ca atoms of helix M3 and M4 of chain A

	Lily LC	Lily Open	GABAAR	GlyR
Lily LC	0,00	1,32	1,31	4,81 ± 0,0
Lily Open (model)	1,32	0,00	1,22	4,83 ± 0,0
GABAAR	1,31	1,22	0,00	4,81 ± 0,0
GlyR (15 struct.)	4,81 ± 0,06	4,83 ± 0,07	4,81 ± 0,05	0.54 ± 0,2

RMSD based on Ca atoms of helix M1,M2,M3 and M4 of the whole pentamer

	Lily LC	Lily Open	GABAAR	GlyR
Lily LC	0,00	1,73	3,17	5,72 ± 0,
Lily Open (model)	1,73	0,00	2,02	5,92 ± 0,
GABAAR	3,17	2,02	0,00	5,63 ± 0,
GlyR (15 struct.)	5,72 ± 0,07	5,92 ± 0,07	5,63 ± 0,09	0,62 ± 0,

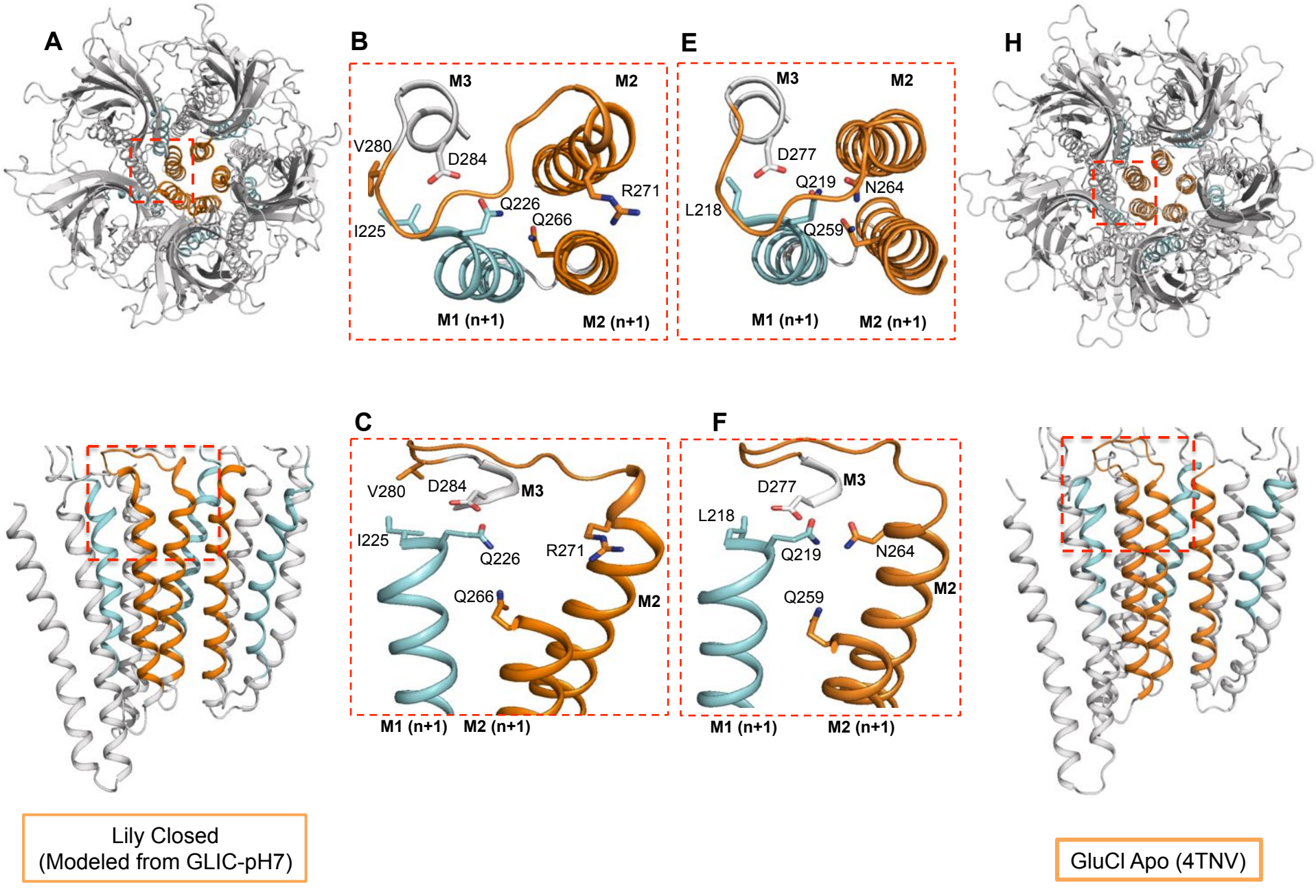

Lily Closed
(Modeled from GLIC-pH7)

GluCl Apo (4TNV)

Table 1. Data collection and refinement statistics

	Lily
Data collection	
Space group	$P2_12_12_1$
Cell dimensions	
a, *b*, *c* (Å)	118.9, 132.3, 190.5
α,β,γ, (°)	90, 90, 90
Resolution (Å)	49.4-3.50 (3.68-3.50)
R_{pim}	0.036 (0.638)
R_{merge}	0.065 (1.12)
I / σ(*I*) Resol. at which I/ σ(I)=2	12.8 (1.2) 3.65
Completeness (%)	99.8 (99.9)
Redundancy	4.9 (5.0)
Refinement	
Resolution (Å)	25.0-3.50
No. reflections	38364
R_{work} / R_{free}	25.4/27.1
No. atoms	
Protein	11407
Ligand/ion	9
B-factors	
Protein	174.3
Ligand/ion	168.9
Molprobity Analysis	
Ramachandran favored (%) Ramachandran outliers (%) Molbrobity score[#] R.m.s. deviations	94.8 0.46 100th
Bond lengths (Å)	0.007
Bond angles (°)	0.92

*Values in parentheses are for highest-resolution shell.

[#]100th percentile is the best among structures of comparable resolution; 0th is the worst

Table S2: Properties of Lily and GlyRs wild type and mutants receptors.

-Lily-							-GlyR-					
Receptor	**EC_{50} (M) [H^+]**	**EC_{50} Mut/ EC_{50} WT**	**I_{max} (nA)**	**nH**	**Conduct (pS)**	**n**	**EC_{50} (M) [Glycine]**	**EC_{50} Mut/ EC_{50} WT**	**Imax (nA)**	**nH**	**Conduct (pS)**	**n**
WT	$2.6 \pm 0.5 \times 10^{-7}$	1	1.6 ± 0.31	1.2 ± 0.2	86 ± 2	14	$44 \pm 2 \times 10^{-6}$	1	2.26 ± 0.31	1.7 ± 0.2	90 ± 3	10
Q226E	ND	-	1.2 ± 0.25	-	85 ± 2	6	$4.7 \pm 0.2 \times 10^{-6}$	0.1	1.66 ± 0.3	1.3 ± 0.2	-	6
P250T	$1.2 \pm 0.2 \times 10^{-5}$	46	0.3 ± 0.12	1.3 ± 0.2	-	6	$570 \pm 80 \times 10^{-6}$	13	0.8 ± 0.12	1.3 ±0.2	-	6
G254A	$2.6 \pm 0.2 \times 10^{-7}$	1	1.3 ± 0.31	1.2 ± 0.4	126 ± 3	7	$42 \pm 3 \times 10^{-6}$	1	2.1 ±0.31	1.1 ± 0.4	-	5
Q266E	$8.7 \pm 0.3 \times 10^{-8}$	0.3	1.1 ± 0.28	1.2 ± 0.2	-	6	$14 \pm 2 \times 10^{-6}$	0.3	6.66 ± 0.8	1.4 ± 0.2	-	5
R271Q	$2.8 \pm 0.5 \times 10^{-6}$	10	1.1 ± 0.31	1.3 ± 0.4	56 ± 3	7	$20 \pm 2.5 \times 10^{-3}$*	454	0.98 ± 0.27	1.2 ± 0.4	-	5
K276C	$3.1 \pm 0.2 \times 10^{-5}$*	119	0.2 ± 0.11	1.1 ± 0.4	87 ± 3	7	$3.8 \pm 0.9 \times 10^{-3}$*	86	1.7 ± 0.11	1.3 ± 0.4	-	6
V280M	ND	-	-	-	86 ± 3	5	NP	-	-	-	-	-
Q226E/R271Q	$1.5 \pm 0.2 \times 10^{-4}$*	576	0.6 ± 0.35	1.2 ± 0.2	-	4	$3.1 \pm 0.4 \times 10^{-3}$*	70	2.1 ± 0.3	2.2± 0.3	-	5
Q266E/R271Q	$6.07 \pm 0.3\ 10^{-5}$	233	0.7 ± 0.29	1.1 ± 0.3	-	5	$4.9 \pm 0.6 \times 10^{-3}$*	112	1.96 ± 0.3	1.6 ± 0.2	-	5

*: For these mutants, the plateau response of the D-R curves could not be accurately achieved; ND: Not Determined; NP: Not Performed; all error values are given as +/- standard deviation